Paper for submission to the Geological Society of London Special Publication
"The Role of Volatiles in the Genesis, Evolution and Eruption of Arc Magmas"

Magnetite-bubble aggregates at mixing interfaces in andesite magma bodies

M. Edmonds[1*], A. Brett[1], R. A. Herd[2], M. C. S. Humphreys[3], A. Woods[1]

1. Earth Sciences Department, University of Cambridge, Downing Street, Cambridge CB2 3EQ

2. School of Environmental Sciences, University of East Anglia, Norwich

3. Earth Sciences Department, University of Durham

* Corresponding author me201@cam.ac.uk

ABSTRACT

Magnetite is a particularly favourable site for heterogeneous bubble nucleation in magma and yet only very rarely is evidence for this preserved, owing to the myriad of processes that act to overprint such an association. The possibility of bubble-magnetite aggregates in magmas carries with it interesting implications for the fluid mechanics of magma bodies and for the magma mixing process responsible for the formation of andesites. We use image analysis and statistical methods to illustrate a spatial association between magnetite and bubbles in mafic enclaves. There is a large range in magnetite contents in the enclaves, up to 7.5%, which is related to the porosity of the enclaves, indicating a mechanism of enrichment of the mafic magma in magnetite. In the andesite there is no spatial association between bubbles and magnetite and the magnetite content of the andesite is small. We suggest a mechanism for enclave formation whereby in vapour-saturated magma, bubbles nucleate on magnetite. Upon intrusion into the base of an andesite magma body, these bubble-magnetite aggregates rise and "sweep up" other magnetites, resulting in the accumulation of aggregates at the magma interface. Instabilities lead to the flotation of enclaves, characterised by enrichment in magnetite and bubbles.

There is strong evidence that mafic magmas in arc settings are rich in water. Rare olivine-hosted melt inclusions from Mount Shasta, for example, record H_2O contents of up to 10 wt% (Grove et al., 2003) and data suggest that mafic arc melt inclusions have an average of 4 wt% H_2O (Plank et al., 2013). Aluminium in hornblende hygrometers applied to arc mafic magmas require melt H_2O contents of 4-8 wt% (Ridolfi et al., 2010). The H_2O contents of the cores of pyroxene phenocrysts in equilibrium with andesite from Soufrière Hills Volcano reflect melt H_2O contents of up to 10 wt% (Edmonds et al., 2014), derived from the fractionation of a mafic melt with 4-6 wt% H_2O. Models of "hot zone" processes at the base of the arc crust invoke water-rich magmas being emplaced into the lower crust, their outgassing lowering the solidus of the ambient crust and allowing assimilation of amphibolite and previously emplaced intrusions, leading to the formation of evolved magmas (Annen et al., 2006). It is therefore likely that mafic magmas, during their ascent through the arc crust, are vapour-saturated for most of their passage, carrying with them a population of bubbles of a supercritical fluid containing substantial H_2O. The dissolved and exsolved volatile budget of these mafic magmas is a dominant control on the mechanisms of magma mingling and/or mixing when these magmas underplate, or intrude evolved, long-lived crystal-rich magma bodies in arcs (Huppert et al., 1982, 1986; Bacon, 1986; Nakamura, 1995; Huber et al., 2010). Ultimately, the transfer of these volatiles to the overlying andesitic magmas, and subsequent outgassing prior to and during eruption, controls eruption style, the transport and segregation of metals, and the flux of volcanic gases into the atmosphere. Finding petrological records of exsolved vapour and the process by which mafic magmas interact with cooler evolved magma bodies is challenging (Wallace, 2001; Blundy and Cashman, 2008; Gardner, 2009). Original bubble populations tend to be overprinted in stored and erupted magmas by crystallisation, bubble growth and coalescence, and outgassing (Larsen et al., 2004; Gardner, 2007). If, however, bubbles nucleate preferentially on one particular mineral phase, then this spatial association might provide a means to understand the fluid mechanics of bubbles, and of bubble-mineral aggregates in mafic arc magmas.

Mafic magmas are likely to fractionate amphibole and magnetite throughout the arc crust (Sisson and Grove, 1993; Grove et al., 1982). It is likely, upon vapour saturation of the melt, that bubbles will nucleate on crystals that provide energetically favourable sites. During nucleation, the larger the liquid-mineral wetting angle (**figure 1**), the larger the reduction in surficial energy. In rhyolitic magmas, the liquid-mineral wetting angle for magnetite is 45-50º, compared with 5-25º for felsic silicates (Schafer and Foley, 2002; Gualda and Ghiorso, 2007). Nucleation on magnetite is therefore favoured over any other phase, in both theory and experiment. Extensive heterogeneous nucleation

of bubbles on magnetite has been observed during laboratory magma decompression experiments (Hurwitz and Navon, 1994; Mangan and Sisson, 2000, 2005; Gardner and Denis, 2004; Gardner, 2007; Cluzel et al., 2008; Gardner and Ketcham, 2011). No such association between bubbles and other phases, such as quartz and feldspar, has been observed (Mangan and Sisson, 2000; Gualda and Ghiorso, 2007). It has been shown that the total Gibbs free energy of the bubble-liquid-crystal system is always lower in the case of bubble-crystal attachment over bubble-liquid configurations, meaning that heterogeneous nucleation is always preferred (Gonnerman and Gardner, 2013). Furthermore, as the wetting angle between bubble and mineral increases (**figure 1**), the efficiency of adhesion of bubbles to minerals is decreased (owing to the deformation force required to change the bubble shape from spherical) but the energy barrier to detachment of bubbles from crystals is greatly increased, so that once a bubble is attached, a larger force is required to detach it (Gualda and Ghiorso, 2007). The energy reduction caused by bubble-magnetite attachment is several orders of magnitude greater than that for bubble attachment to other minerals. Furthermore, it has been shown that, theoretically, magnetite grains of several hundred microns in size can be held attached to a bubble by surface forces (Gualda and Ghioso, 2007).

An association between magnetites and a bubble has been recognised previously: a pre-eruptive aggregate of multiple magnetite crystals and a single bubble was observed in a pumice sample from the Bishop Tuff rhyolite (Gualda and Anderson, 2007). This observation prompted suggestion that the formation of magnetite-bubble aggregates might be a mechanism of storing exsolved vapour in a magma reservoir, whereby the magnetite anchors the positively buoyant bubble (Gualda and Ghiorso, 2007). Finding evidence for such an association in erupted magmas is extremely challenging. Shear forces act to detach bubbles from crystals during eruption and during convection in the magma chamber. In addition, pre- and syn-eruptive processes of bubble growth, coalescence and outgassing will usually overprint the spatial link between the two phases, if such a link originally existed. Bearing in mind the ways in which overprinting of textures might occur, it would seem that the most likely magma types within which a spatial link between magnetite and bubbles might be preserved are those that quenched rapidly prior to eruption, such as mafic enclaves chilled against a cooler magma. In this scenario, enclaves may retain the characteristics of the original bubble and magnetite populations without significant modification.

We studied samples erupted from Soufrière Hills Volcano, Montserrat in 2007. The eruption (1995-2011; Wadge et al., 2014) was characterised by crystal-rich andesite (with a rhyolitic melt), with up

to ~ 10 vol% mafic enclaves (Murphy et al., 2000; Barclay et al., 2010; Plail et al., 2014). The andesite exhibits petrological evidence for recent heating, in the form of sieve-textured plagioclase, opaticized amphibole, reverse-zoned orthopyroxene, and resorbed quartz (Murphy et al., 2000; Humphreys et al., 2009a). Melt inclusions in plagioclase in the andesite contain up to 6.3 wt% H_2O and a few hundred ppm CO_2 (Humphreys et al., 2009b; Edmonds et al., 2014). Compositional zoning at the rims of titanomagnetite in contact with ilmenite suggests that at least the latest stage of heating might have taken place weeks-months before eruption (Devine et al., 2003). Geophysical observations of strain and ground deformation, as well as numerical modelling of magma flow, place constraints on the form of the plumbing system (Elsworth et al., 2008; Fooroozan et al., 2010; Hautmann et al., 2009). A coupled magma reservoir system exists at depth, with one magma storage area at around 12 km and one shallower, at around 5-7 km. The shallow chamber is connected to the surface via a dyke (Costa et al., 2013). Studies of volcanic gas emissions from Soufrière Hills Volcano have invoked largely unerupted mafic magma (perhaps the magma erupted in the form of enclaves) as the source of the sulphur gas emissions (Edmonds et al., 2001; 2010). Mafic enclaves have a diktytaxitic texture, indicative of rapid quenching against a cooler magma (Bacon 1986; Clynne, 1999; Martin et al., 2006) and a porosity of up to 40 vol% (Edmonds et al., 2014). Phase equilibria and amphibole compositions suggest water concentrations of up to 6-10 wt% (Edmonds et al., 2014). Mafic enclaves exhibit a range of textural and compositional types, ranging from basaltic enclaves with glassy margins to more crystalline enclaves of basaltic andesite composition (Plail et al., 2014).

In this paper, we look for evidence that bubbles nucleate on magnetite in the magma reservoir beneath the Soufrière Hills Volcano. We use image analysis and statistical techniques on backscattered electron images to assess whether there is an association between magnetites and bubbles, or bubbles and other phases, in the erupted andesitic lavas and in mafic enclaves. We investigate the implications of such an association for understanding the behaviour of magnetite-bubble aggregates and magma mingling and the fluid mechanics of the basaltic magma at the interface with the andesite.

METHODOLOGY

We use statistical analysis of the spatial distribution of grains in 2D back-scattered electron images to investigate whether there is any relationship between the positions of magnetite grains and bubbles in the samples. Methods are described in detail below.

132

133 *Samples*

134 Samples for this study are andesitic blocks with porosity of up to 25 vol% in pyroclastic flow
135 deposits (**table 1**). The lava blocks were sampled from the January 2007 Belham River pyroclastic
136 flow deposit. The lava blocks have mafic enclaves up to 25 cm in dimension but more commonly <
137 5 cm (Plail et al., 2014; **figure 2**), with a porosity of up to 25 vol%. The andesite blocks have been
138 degassed to variable degrees and the porosity structure has been affected undoubtedly by bubble
139 coalescence, outgassing and collapse (Klug and Cashman, 1996; Giachetti et al., 2010). The mafic
140 enclaves, however, display glassy quenched rims and porosities up to 25 vol% (Edmonds et al.,
141 2014), raising the possibility that they preserve a greater proportion of their original porosity
142 structure that existed prior to eruption. The sample names have a hierarchy that relate to individual
143 hand specimens from blocks in the flow deposit, i.e. BR6_x where x is 1, 2 and 3 are three samples
144 from the same hand specimen. Pumice samples were not used in this study as the exceedingly high
145 vesicularity meant that crystals were too sparse and bubbles not separated sufficiently for
146 meaningful statistical analysis.

147

148 *Scanning electron microscope images and image analysis*

149 The images were acquired using a JEOL JSM-820 Scanning Electron Microscope (SEM) operating
150 at an accelerating voltage of 20kV (Earth Sciences, Cambridge). The software ImageJ was used to
151 characterise the resulting images. Magnetite and vesicles were isolated by setting appropriate
152 greyscale value thresholds, which were then quantified using the "Analyze Particles" function. For
153 every particle, area (minimum, mean and maximum grey values), centroid, centre of mass, and
154 perimeter length were recorded. Measurements were made with two minimum particle sizes (areas
155 of 10 pixel units and 50 pixel units). The 10 px-thresholded analyses contained many more spurious
156 results (e.g. of cracks or dust). As a consequence, the 50 px-thresholded analyses were used for the
157 statistical analysis, which introduced a systematic failure to sample the smallest particles. However,
158 the choice of this larger minimum size meant that most of the cracks and holes inside phenocrysts
159 were avoided. There remains a small fraction of these voids in the interior of crystals (<<1% of total
160 particles) that have been recorded as points in the populations, but these do not change the form of
161 the statistical plots. Sampling bias was also introduced by the size of the thin sections: there is a
162 potential bias away from the very largest vesicles, which exceed 0.5 cm in size. The backscatter
163 images also vary in their magnification, resulting in a variable pixel size ranging from 0.14 microns
164 to 2.25 microns (**table 1**), which may also affect results. The centroid positions of orthopyroxenes

was also recorded for sample MVO1560_1 to test the null hypothesis that bubbles are related equally well spatially to all phases. Representative backscatter images of the andesite and of the mafic enclaves, with the phases labelled, are shown in **figure 3**.

Statistical analysis

The aim of the statistical analysis is to evaluate whether two populations are spatially clustered i.e. whether their locations are dependent upon one another. In the petrological literature, there are many examples of studies aiming to assess clustering and the spatial characteristics of single populations of phases (e.g. Jerram et al., 1996; Jerram et al., 2003; Higgins and Chandrasekharam, 2007); far fewer attempting to assess the spatial dependence of multiple populations of phases. The traditional statistic used to evaluate clustering is the aggregation index, R, of Clark and Evans (1954) and later Kretz (1966), Boorman et al (2004), Higgins (2006) and Jerram et al. (1996, 2003). The R index is based on the nearest neighbour distances:

$$R = \frac{r_A}{r_E} \quad (1)$$

where r_A is the mean of the distances separating points from their nearest neighbours, and r_E is the expected value of r_A for complete spatial randomness. By definition, R=1 for complete spatial randomness. If the points are clustered, the distance to nearest neighbours is shorter than that expected for complete spatial randomness and R<1. Conversely, if points are ordered (with points further away than expected for spatial randomness), R>1. The nearest neighbour distance distribution function of a point pattern is the cumulative distribution function $G(r)$ of the distance r from a typical random point to the nearest other point of the population, given by

$$G(r) = 1 - exp(-\lambda \pi r^2) \quad (2)$$

where λ is the intensity, or the number of points per unit area. The drawback of using the R index, and nearest neighbor statistics, however, is that it is "short-sighted" and cannot characterise particle spatial patterns further away than the nearest neighbor. It cannot distinguish, for example, between complete spatial randomness and the case with both clustering and ordering on different length scales, since R=1 in both cases (Rudge et al., 2008).

196

197 Instead of nearest neighbor analysis alone, we have chosen to use a range of statistical methods
198 based on Ripley's K Function, $K(r)$, calculated using Spatstat, a statistical package that uses R as a
199 platform. The pair correlation function (or radial distribution function) $g(r)$ is defined as

200

201 $$g(r) = \frac{1}{2\pi r}\frac{dK(r)}{dr} \quad (3)$$

202

203 where

204

205 $$K(r) = \frac{E(\#\text{ extra events within distance r of a randomly chosen event})}{\lambda} \quad (4)$$

206

207 and where λ is the number per unit area of particles. The parameter $L(r)$, a transformation of
208 $K(r)$, is defined as

209

210 $$L(r) = \sqrt{\frac{K(r)}{\pi}} \quad (5)$$

211

212 For a completely random (uniform Poisson) point pattern, the theoretical value of the L-function is
213 $L(r) = r$, yielding a straight line with a positive slope on a plot of $L(r)$ against r (e.g. **figure 4**).

214

215 The pair correlation function allows a more complex analysis of ordering and clustering on multiple
216 length scales, instead of being confined to the nearest neighbour. The value $g(r)$ determines how
217 likely an inter-point distance of r is: $g(r)$ is equal to 1 for complete spatial randomness. If $g(r) > 1$
218 then it is more frequent than complete spatial randomness; if $g(r) < 1$ then it is less frequent than
219 complete spatial randomness (e.g. **figure 4**). Edge effects are taken into account. These arise when
220 incomplete grains near the edge, whose centroids fall within the bounding box, are not counted,
221 leading to fewer grains near the edge, which biases all the statistics. Another source of error is that
222 nothing is known about grains outside of the window under consideration: a grain may have a
223 nearest neighbor just outside the window, for example, instead of the grains that are visible inside
224 the window (Rudge et al., 2008). To correct for this latter effect, a buffer zone is introduced around

the edge of the observation window where nearest neighbour distances are not calculated, but the points are available as neighbours for the points in the inner region (Clark and Evans 1954). The buffer zone should be large enough so that the nearest neighbours of points in the inner region can always be found either in the inner region or in the buffer zone. Choosing the size of the buffer zone is critical: too large and valuable data is discarded; too small and edge effects remain (Rudge et al., 2008).

Synthetic point patterns

Synthetic distributions were generated to provide validation data for our investigation (**figures 4, 5**) and are divided into two groups. Independent populations (**figure 4**) are two separate populations (*A* and *B*) superimposed upon one another, where the individual points of each (*i* and *j*) have no spatial link or dependence; the populations may be random (poisson), clustered (gaussian) or ordered. Random populations were generated using a random number generator, with specified average intensity (point density). Clustered populations were generated using a number of random seed positions and specified cluster densities (we use "strong" and "weak" cluster densities with effects similar to those observed in natural distributions) and cluster dimensions, with a Gaussian distribution around the seed point. Ordered distributions are generated using a self-avoiding algorithm, whereby the image space is populated sequentially by points using the maximum distance from all existing neighbouring points.

For each synthetic point pattern, cumulative probability distributions to show nearest neighbour distances, Ripley's L function, and the pair correlation function, were generated (**figure 4**). For random population pairs that are not spatially linked (**figure 4a**), nearest neighbour cumulative probability plots show no difference from the data generated from the random simulations (grey envelope). For the rest of the independent pattern nearest neighbour plots, in general the nearest neighbour distances are longer than predicted for the random pair pattern simulations (i.e. there is a marked absence of short nearest neighbour distances), with the exception of random-ordered (**figure 4b**) and ordered-ordered (**figure 4e**), which show an absence of the longer distances, consistent with the ordering of at least one of the particle populations. In contrast, the plots of the cumulative Ripley's L Function shows that, without exception, when the two point patterns are spatially independent, regardless of point pattern "type" there is no statistical difference between simulations on two random point patterns, and the data generated from the synthetic pattern. The pair correlation function, which is essentially the non-cumulative form of the Ripley's L function,

shows essentially the same thing. The departures at small r reflect the nearest neighbour deviations from random behaviour. Importantly though, the medium and far-field are no different to the statistics generated from random simulations (the grey envelope), and this is true for all of the independent population point patterns in **figure 4**. The wave-like features at the larger distances have a wavelength proportional to cluster intensity, or ordering intensity. The only pattern showing a slightly stronger signal (a slight departure from random in Ripley's L function, and a positive excursion from random in the pair correlation function) is the synthetic pattern showing two independent clustering patterns (weak and strong; **figure 4i**). This may be an artefact arising from the particular point pattern generated. In order to establish the source of these data it would be necessary to run multiple analyses on a number of different clustering patterns. For the purposes of this analysis, however, it can be seen the departures from random for these independent population synthetic patterns in the medium and far field are small and of no consequence.

Linked, or dependent, populations are generated using common seed points (**figure 5**). For example, for a linked random-randomised two population synthetic pattern (**figure 5i**), population *A* is a random (poisson) distribution of points *i*, population *B* is defined as having individual points *j* (B_j) shifted from A_i, using random vectors from each point *i*, using a specified number of pixels as available sites around A_i. For a linked ordered-clustered two population synthetic pattern, a random subset of the ordered point pattern points *i* of population *A* is used as seeds for the clusters in point pattern *B* defined by points *j*. Each point pattern contains 1000 points.

For each pair of dependent point patterns, statistical data for nearest neighbour, Ripley's L function, and the pair correlation function (pcf) were generated (**figure 5**). The statistical data show quite striking differences to the independent patterns shown in **figure 4**. Paired clustered populations have nearest neighbour cumulative probability distributions strongly skewed to small distances (**figure 5a-c**). Ordered-clustered paired populations show the opposite: distributions skewed to large distances, with the smallest distances absent (**figure 5d, e**). However, there are very large positive deviations at very small r (<0.1), caused by the way that the second populations uses seeds derived from the first population. This strong positive deviation is observed in almost all of the dependent synthetic patterns and is also expected to occur in natural populations if they are strongly spatially linked. The ordered and random populations with the second population "randomised" around points of the first (**figure 5e, f**) show a larger fraction of smaller distances than the random case. For the Ripley's L function plots, which consider particles further away than the nearest neighbour,

significant departures from random behaviour are only observed when the two populations exhibit paired clustering, i.e. when the two populations are clustering in the same place (**figure 5a-c**). The pair correlation function shows positive and broad departures from random behaviour. The random-randomised results (a random first population, with the second population paired with it so that one particle of the second population is randomly distributed around each particle of the first; **figure 5i**) show an effect similar to the paired clustered populations above, albeit slightly weaker. There is a positive excursion from random in both nearest neighbour and Ripley's L function, and a similarly shaped pair correlation function plot (**figure 5i**). When one population is ordered, the pair correlation function plots show a negative deviation from random behaviour at distances of <1, caused by the self-avoiding algorithm used to generate the ordered populations. This might arise in the natural population when there are other phenocrysts, for example, which act to separate the two populations in a systematic way, or when the two populations particle sizes have a finite minimum size.

The effect of changing the order of the analysis was also investigated (**figure 6**), for the cases of the dependent synthetic populations clustered-randomised and random-clustered. In the first case (**figure 6a**), the first population is clustered; this might represent clustered magnetites, for example. The second population nucleates preferentially upon the first, resulting in two clustered populations. This might represent bubbles nucleating on clustered magnetites, with the result being that magnetites and bubbles are both clustered, with common seed points. The spatial statistics show strong clustering in nearest neighbour distances, Ripley's L and the pair correlation function. In the second case, the first population is random and the second population nucleates preferentially upon the first. This represents the case where magnetites are distributed randomly and bubbles nucleate on them. The spatial statistics in this case are very different; clustering behaviour is only observed at small distances, with ordering at intermediate distances. These two cases might just as easily, of course, represent magnetites nucleating on clustered bubbles (**figure 6a**) and magnetites nucleating on randomly distributed bubbles (**figure 6b**). We regard this as slightly less likely than the case where magnetite is the first population. We can therefore discriminate, from the synthetic data, whether the first population is clustered or randomly distributed.

The results of these simulations show, unequivocally, that two independent populations can be distinguished from the case where the two populations are linked spatially. Furthermore, the nature of the linkage can be established in some cases: where both populations are clustered with common

seed points, this results in a very characteristic set of spatial statistics, most categorically in Ripley's L function. Comparison between the statistics generated from the natural data, with these results from the synthetic patterns, allows discrimination between these scenarios.

RESULTS

Magnetite and vesicle size and area distributions

Representative backscatter images of the vesicular andesite lava, breadcrust bombs and mafic enclaves are shown in **figure 3**. The size distributions of bubbles and magnetite grains are shown in **figure 7** as kernel density estimates (generated using the ksdensity normal kernel smoothing function in Matlab). The sample types (andesite or mafic enclave) are listed in **table 1** and marked on **figure 7**. In general, the vesicles in the mafic enclaves have larger modal sizes and broader size distributions, ranging to larger vesicle sizes. However, the more crystalline mafic enclaves (e.g. BR11, MVO 1592 1) have narrower peaks in the vesicle size distribution at smaller sizes, more similar to the andesite (**figure 7**). There are no clear differences in terms of magnetite size distribution between mafic enclaves and andesite samples. Modal bubble sizes range from 20-40 microns, with some mafic enclave samples showing significant positive skew in the distribution, with tails extending up to 200-250 microns (*e.g.* MVO 1587 2, MVO 1592 4). Magnetite grains have a modal size of typically 25-60 microns, with the largest grains occurring in mafic enclave sample MT19 1. The grain size distributions are positively skewed, with a larger than expected proportion of larger crystals in the size range 100-300 microns. In almost all cases, the magnetite and vesicle sizes are coupled, such that the distributions show similar magnitudes and shapes for a single sample.

There is a large range in the area fraction of magnetite in the mafic enclave images, which reaches 7.5 % (**figure 8**), which is in contrast to the andesite samples, which have magnetite area fractions up to *c.* 2 %. Vesicle area fractions range between 12 and 24 % in the mafic enclaves, and 2-23 % in the andesite samples. These values for vesicle area fraction are consistent with previous work for Soufrière Hills (Edmonds et al., 2014) and with work on bubble growth, outgassing and bubble collapse recorded in other similar dome-forming magmas (e.g. Stasiuk et al., 1996; Hammer et al., 2000; Scheu et al., 2006). There is a weak negative correlation between vesicle area fraction and magnetite area fraction (**figure 8**), which may indicate a genetic link between the two phases.

356 *Two population (bubble-magnetite) statistics*

357 **Figures 9, 10 and 11** show the point patterns and the statistics generated from the natural data,
358 which are shown as backscatter images at the far left of the figure. Representative andesite samples
359 are shown in **figure 9,** which shows, without exception, that there is no significant departure from
360 random behaviour in the nearest neighbour plots. The large negative deviations at small r (<20
361 microns) are likely due to the finite size of the magnetites and vesicles (**figure 7**), which imposes
362 ordering. All of the samples shown display a small positive deviation from random in the Ripley's
363 L and pair correlation functions at distances 20-200 microns (**figure 9**), consistent with dependent
364 clustering or dependent random populations (**figure 5**). The andesite pair correlation function data
365 are isolated and shown in red in **figure 11**, with the theoretical random distribution shown at 1, as
366 well as a grey envelope to show the region in which the results of 100 random simulations plot.
367 Overall the statistical data for the andesite plots showing little near field and only weak medium
368 field spatial linkage between magnetites and vesicles in the images.

369

370 Representative data for the images that show parts of mafic enclaves are shown in **figure 10**. These
371 data are markedly different from the andesite data in **figure 9**. Nearest neighbour plots consistently
372 show a mode at higher distances than for the random case, characteristic of clustered populations,
373 but not conclusive in showing that the populations are paired. However, the Ripley's L function
374 plots for the enclaves show varying degrees of strong positive excursions from the random case,
375 particularly for r<100 μm, indicating that both populations are clustered (from comparison with
376 **figure 5** and from the analysis shown in **figure 6**), and further, that they are spatially dependent
377 upon one another, sharing common seed points. This paired, clustered relationship is also shown in
378 the pair correlation function plots, which show a strong positive and broad shape. The comparison
379 between the enclave and andesite pair correlation function with particle distance is shown in **figure**
380 **11**. The data for the mafic enclaves are significantly different to the andesite and furthermore,
381 significantly different from the envelope defined by the results of 100 random simulations, which is
382 not the case for the andesite data. The mafic enclave pair correlation function plots also show
383 negative deviations from random behaviour at r< 30 microns, consistent with the bubble and
384 magnetite sizes (**figure 7**), which imposes a minimum limit on particle separation and apparent
385 ordering.

386

387 To summarise, the statistical data for the mafic enclaves show that the first population of particles
388 (magnetite) shows significant clustering, leading to linked clustered behaviour in the vesicle

distribution also. The andesite shows only a very weak spatial linkage between the two populations. The results of the pyroxene-bubble paired analysis are shown in **figure 12**. For this particular image, there is no spatial relationship between bubbles and orthopyroxene.

DISCUSSION

The results of this study show that magnetite and bubble sizes are coupled in all samples studied (**figure 7**). There is a large range in mafic enclave magnetite contents, which is related weakly to the vesicularity of the samples (**figure 8**). In the andesite samples, the area fraction of magnetite varies very little, up to 2%. We propose that the variation in vesicularity with magnetite content is linked with enclave bulk composition, as shown in previous studies (Edmonds et al., 2014; Plail et al., 2014). The enclaves may be classified into one of two types: A and B (Plail et al., 2014). Type A is more mafic in bulk composition (basaltic) and contains mainly hornblende and plagioclase as phenocryst phases. Vesicularity is high, the groundmass is glassy and the enclaves typically have quenched margins. The most vesicular enclaves in **figure 8**, with the lowest magnetite contents, are of this type. Type B enclaves range to basaltic andesite in bulk composition, and contain plagioclase, pyroxene and oxides as phenocryst phases. They have lower vesicularity and a crystalline groundmass, with no quenched margin; we propose that the lower vesicularity enclaves on **figure 8** are of this type. Type B enclaves have almost certainly lost a substantial portion of their porosity through outgassing, as suggested by their higher degree of bubble coalescence and absence of quenched glassy margins (Edmonds et al., 2014; Plail et al., 2014).

There is evidence of clustering in the mafic enclave samples, both within the single populations of magnetite and bubbles, and in the paired populations, which are spatially dependent upon one another. There is no evidence that bubbles are linked spatially with other crystal phases such as orthopyroxene (**figure 12**). In the andesite, however, there is no clear relationship and the populations are either independent or very weakly dependent. The individual populations are either random or slightly clustered, with varying degrees of ordering, likely imposed by the phenocryst phases present. The absence of a strong clustering between magnetites and bubbles in the andesite might be explained by overprinting of the association during magma ascent, degassing and rheological stiffening. We envisage that the shear forces generated during magma flow are likely to exceed the attachment forces between bubbles and magnetites, hence obliterating any association. The mafic enclaves are protected from such shear forces due to their coherence and their crystal frameworks, which makes them strong (Martin et al., 2006). Alternatively or in addition, the lower

magnetite content in the andesite might promote a greater proportion of bubble nucleation on other phases (Cluzel et al., 2008). We discuss the possible causes of the linked populations of bubbles and magnetite in the enclaves and the implications for the fluid mechanics of the system.

The origin of magnetite-bubble aggregates in mafic arc magmas

The clustering between magnetite and vesicles could be due to either magnetite nucleation on bubble walls, owing to short lengthscale changes in melt oxidation state and oxygen fugacity during degassing (Humphreys et al. in review; Moussallam et al. 2014), or to bubble nucleation on magnetite. Our results are consistent with both heterogeneous nucleation of bubbles on magnetite grains and a mechanism whereby bubbles "sweep up" magnetites during rise through melt. Of the crystal phases commonly present in arc settings, magnetite provides by far the most energetically favourable surface for heterogeneous nucleation of bubbles. Experiments show strong evidence for heterogeneous nucleation on all surfaces of magnetite, with no other minerals serving as nucleation sites during decompression (Gardner and Denis, 2004; Gardner, 2007; Cluzel et al. 2008; Gardner and Ketcham, 2011). Hurwitz and Navon (1994) developed a theoretical model of the relationship between liquid-mineral wetting angle and supersaturation, such that higher wetting angles favour heterogeneous over homogeneous nucleation. Gualda and Ghiorso (2007) show that in rhyolitic melts the attachment energy for magnetite-bubble aggregates is much greater than for silicate mineral-bubble aggregates. This is due to the significantly greater liquid-mineral wetting angles: 45-50 degrees for magnetite, versus 5-25 degrees for felsic silicates (**figure 1)**. The reduction in surface energy resulting from bubble-mineral attachment is at least one order of magnitude greater for magnetite than for any silicate mineral.

Clustering between magnetite and bubbles may be explained by heterogeneous nucleation of bubbles on magnetite, but also by bubbles "sweeping up" magnetites (**figure 13**; Belien et al., 2010). The latter mechanism involves rising bubbles coming into contact with magnetite grains: the reduction in surficial energy may be sufficient to stall the bubbles, with larger bubbles being split by the grains, which would influence their buoyancy. The range in total magnetite content would support this "sweeping up" mechanism, although this mechanism would intuitively lead to a positive correlation between vesicularity and magnetite content, which is not seen. It is likely, however, that these kinds of relationships would be very easily overprinted by outgassing of the magma during quenching and/or decompression.

454

455 *Implications of magnetite-bubble aggregates for the fluid mechanics of the system*

456 The presence of bubble-magnetite aggregates has fundamental implications for the degassing
457 process by promoting heterogeneous over homogeneous nucleation, further favouring equilibrium
458 degassing, low bubble number densities and affecting processes of bubble growth and coalescence
459 (e.g. Gardner, 2009). Regardless of how bubble-magnetite aggregates form, their existence might
460 also give rise to a number of complex behaviours in the magma reservoir. For example, if the
461 overall bulk density of the magnetite-bubble aggregate is higher than the surrounding rhyolitic melt,
462 the aggregate will sink (if the yield stress is overcome). Increasing pressure will tend to compress
463 the bubble further, accelerating the aggregate's fall as a positive feedback mechanism. The system
464 is possibly unstable in both directions so that some crystals may sink, and others may rise to the top
465 of the chamber, depending on the pressure difference between top and base of chamber. If gas-
466 crystal pairs are neutrally buoyant at some level in the magma chamber and are moved downwards,
467 the pressure increase will cause bubble shrinkage and hence the density goes up fractionally and the
468 aggregate will sink. Conversely if the aggregate rises a little, it will allow bubble expansion and the
469 pair then becomes buoyant and will continue upwards. Hence it would not be possible dynamically
470 to have an intermediate layer of bubble-crystals unless the surrounding melt is stratified (i.e. the
471 density of fluid above the crystal-bubble pairs is lower by a finite amount and the density of the
472 fluid below is greater). The presence of bubble-magnetite aggregates should therefore lead to
473 magnetite-rich layers both at the floor and the roof of the chamber. Abundant clots of magnetite +
474 orthopyroxene + apatite + vesicles ± plag exist in the andesite (Humphreys et al., 2009), perhaps
475 remobilised from crystal mushes at the floor and roof of the magma chamber.
476

477 The large reduction in surficial energy available via formation of bubble-magnetite aggregates
478 suggests that bubbles are extremely likely to attach to magnetite grains they interact with
479 ("magnetite scavenging"). As bubbles rise they expand due to decompression, with further
480 expansion due to bubble coalescence and continuing exsolution. The increase in rise speed due to
481 increased buoyancy is counteracted by the greater likelihood of encountering more dense magnetite
482 grains, which have the effect of slowing the aggregate down, and the greater difficulty of passing
483 through the more crystal- and aggregate-rich magma. This mechanism might "trap" aggregates in
484 regions of dense crystals ("mushes") and hence be a mechanism to store exsolved vapour, in the
485 manner illustrated by the recent experiments of Belien et al., (2010).

486

In order to explain the links between bubbles and magnetites in the mafic enclaves, we propose the following conceptual model (**figure 13**) to explain our observations. Intruding mafic melts (>1000 °C; Humphreys et al., 2009a) are significantly hotter than resident andesite magma (~830 °C, Humphreys et al., 2009a). If the mafic magma was H_2O-rich, with >6 wt% H_2O (on the basis of Rhyolitemelts modelling to reproduce the crystal assemblage; Edmonds et al., 2014), the mafic magma may have become vapour-saturated at >300 MPa in the arc crust. At this pressure magnetite, amphibole and orthopyroxene are likely liquidus phases (e.g. Davidson et al., 2007). Much of the bubble population would have nucleated on magnetite crystals. Upon intrusion into the base of the long-lived andesite magma reservoir (**figure 13**), bubble-magnetite aggregates were able to rise relative to the surrounding melt, as a consequence of both the low bulk viscosity of the melt and bubble expansion. The bubble-magnetite aggregates "swept up" more magnetite grains during their ascent, and the aggregates accumulated at the interface between the two magmas. There was probably little pervasive leakage and mixing between the two magmas owing to the large contrast in viscosity (Huppert et al., 1984, 1986; Phillips and Woods, 2001; 2002; Ruprecht et al., 2008), although the mafic magma, being around 150° C hotter than the andesite magma, quench crystallised to form the diktytaxitic texture characteristic of the enclaves (Murphy et al., 2000; Plail et al., 2014). A fraction of the vesicularity in the enclaves, perhaps a large fraction, is a result of quench crystallisation and vesiculation at the interface. Enclaves formed at the interface due to gravitational instabilities of the type proposed by Thomas et al. (1993). The enclaves preserved their magnetite and bubble-rich composition, as well as a texture indicating rapid crystallisation and further vesiculation at the interface. The range in magnetite contents probably reflects local variability in the concentration of aggregates at the interface; or perhaps reflects mixing with the host andesite in a "hybrid zone" at the interface, as suggested by Plail et al., (2014) to explain the geochemistry of the enclaves.

CONCLUSIONS

- We have used image analysis and statistical methods to illustrate a spatial association between magnetite and bubbles in the interior of mafic enclaves erupted in andesite lava blocks at Soufrière Hills Volcano. There is a large range in magnetite contents in the mafic enclaves, up to 7.5 % by volume, which is related to the porosity of the enclaves, indicating a genetic link between the two phases and a mechanism whereby enrichment of the mafic magma in magnetite occurs. In the crystal-rich andesite there is no or only a very weak spatial association between bubbles and magnetite. The total magnetite content of the andesite is lower (0.2-1.2 vol%).

- This study is the first to illustrate a statistical association between magnetite and bubbles in a volcanic rock and confirms the theoretical predictions which state that magnetite is a particularly favourable site for heterogeneous bubble nucleation in magma.
- The possibility of bubble-magnetite aggregates in magmas carries with it interesting implications for the fluid mechanics of magma chambers, involving the ability of magma bodies to "store" exsolved vapour, the formation of cumulates and crystal-rich mushes, and their remobilisation potential.
- We suggest a mechanism for enclave formation whereby water-saturated mafic magma nucleates bubbles on magnetite, which is a liquidus phase deep in the arc crust. Upon intrusion into the base of an andesite magma body, bubble-magnetite aggregates rise and "sweep up" other magnetite grains, resulting in the accumulation of bubbles and magnetite crystals at the magma interface. Instabilities lead to the flotation of enclaves, which are characterised by enrichment in magnetite and bubbles.

ACKNOWLEDGEMENTS

Melissa Plail (University of East Anglia) supplied some of the mafic enclave samples used in this study. Rachel Ledden (University of Cambridge) acquired some of the backscattered electron images. MCSH acknowledges support from a Royal Society University Research Fellowship. We thank Caroline Martel and an anonymous reviewer for their comments, which improved the manuscript.

BIBLIOGRAPHY

ANNEN, C., BLUNDY, J. D. & SPARKS, R. S. J. 2006. The genesis of intermediate and silicic magmas in deep crustal hot zones. Journal of Petrology 47, 3, 505–539.

BACON, C. R. 1986. Magmatic inclusions in silicic and intermediate volcanic rocks. Journal of Geophysical Research, Solid Earth B6, 6091–6112.

BARCLAY, J., HERD, R. A., EDWARDS, B., KIDDLE, E. & DONOVAN, A. 2010. Caught in the act: Implications for the increasing abundance of mafic enclaves during the eruption of the Soufrière Hills Volcano, Montserrat. Geophysical Research Letters, 37, 19.

BELIEN, I.B., CASHMAN, K.V. & REMPEL, A.W. 2010. Gas accumulation in particle-rich suspensions and implications for bubble populations in crystal-rich magma. Earth and Planetary Science Letters, 297, 133–140.

BLUNDY, J. & CASHMAN, K. V. 2008. Petrologic reconstruction of magmatic system variables and processes. Reviews in Mineralogy and Geochemistry 69, 1, 179–239.

BOORMAN, S., BOUDREAU, A., & KRUGER, F. J. 2004. The lower zone–critical zone transition of the Bushveld Complex: a quantitative textural study. Journal of Petrology, 45, 6, 1209–1235.

CLARK, P.J. & EVANS, F.C. 1954. Distance to nearest neighbor as a measure of spatial relationships in populations. Ecology, 35, 445–453.

CLUZEL, N, LAPORTE, D., PROVOST, A. & KANNEWISCHER, I. 2008. Kinetics of heterogeneous bubble nucleation in rhyolitic melts: implications for the number density of bubbles in volcanic conduits and for pumice textures. Contributions to Mineralogy and Petrology, 156, 745–763.

CLYNNE, M. A. 1999. A complex magma mixing origin for rocks erupted in 1915, Lassen Peak, California. Journal of Petrology 40, 1, 105–132.

COSTA, A., WADGE, G., STEWART, R., & ODBERT, H. 2013. Coupled subdaily and multiweek cycles during the lava dome eruption of Soufrière Hills Volcano, Montserrat. Journal of Geophysical Research, Solid Earth, 118, 5, 1895–1903.

DAVIDSON, J., TURNER, S., HANDLEY, H., MACPHERSON, C. & DOSSETO, A. 2007. Amphibole "sponge" in arc crust? Geology 35, 9, 787–790.

EDMONDS, M., AIUPPA, A., HUMPHREYS, M. C. S., MORETTI, R., GIUDICE, G., MARTIN, R. S., HERD, R. A. & CHRISTOPHER, T. 2010. Excess volatiles supplied by mingling of mafic magma at an andesite arc volcano. Geochemistry Geophysics Geosystems, 11:doi:10.1029/2009GC002781, 2010.

EDMONDS, M., HUMPHREYS, M. C. S., HAURI, E. H., HERD, R. H., WADGE, G., RAWSON, H., LEDDEN, R., PLAIL, M., BARCLAY, J., AIUPPA, A., CHRISTOPHER, T., GUIDICE, G. & GUIDA, R. 2014. Pre-eruptive vapour and its role in controlling eruption style and longevity at Soufrière Hills Volcano. In: The eruption of Soufriere Hills Montserrat from 2000 to 2010. Eds G. Wadge, R. Robertson, B. Voight. Geological Society, London, Memoirs, 39, 289–313.

ELSWORTH, D., MATTIOLI, G., TARON, J., VOIGHT, B. & HERD, R. 2008. Implications of magma transfer between multiple reservoirs on eruption cycling. Science, 322, 5899, 246–248.

GARDNER, J. E. & DENIS, M.-H 2004. Heterogeneous bubble nucleation on Fe-Ti oxide crystals in high-silica rhyolitic melts. Geochimica et Cosmochimica Acta 68, 17, 3587–3597.

585 GARDNER, J.E. 2007. Heterogeneous bubble nucleation in highly viscous silicate melts
586 during instantaneous decompression from high pressure. Chemical Geology 236, 1, 1–12.

587 GARDNER, J.E 2009. The impact of pre-existing gas on the ascent of explosively erupted
588 magma. Bulletin of Volcanology, 71, 835–844.

589 GARDNER, J.E & KETCHAM, R. A. 2011. Bubble nucleation in rhyolite and dacite melts:
590 temperature dependence of surface tension. Contributions to Mineralogy and Petrology, 162, 929–
591 943.

592 GONNERMANN, H. M. & GARDNER, J. E. 2013. Homogeneous bubble nucleation in
593 rhyolitic melt: Experiments and nonclassical theory. Geochemistry, Geophysics, Geosystems 14,
594 11, 4758–4773.

595 GROVE, T. L., ELKINS-TANTON, L. T., PARMAN, S. W., CHATTERJEE, N.,
596 MÜNTENER, O., & GAETANI, G. A. 2003. Fractional crystallization and mantle-melting controls
597 on calc-alkaline differentiation trends. Contributions to Mineralogy and Petrology, 145, 5, 515–533.

598 GROVE, T. L., GERLACH, D. M., & SANDO, T. W. 1982. Origin of calc-alkaline series
599 lavas at Medicine Lake volcano by fractionation, assimilation and mixing. Contributions to
600 Mineralogy and Petrology 80, 2, 160–182.

601 GUALDA, G. A. R. & ANDERSON, A. T. 2007. Magnetite scavenging and the buoyancy
602 of bubbles in magmas. Part 1: Discovery of a pre-eruptive bubble in Bishop rhyolite. Contributions
603 to Mineralogy and Petrology, 153, 733–772.

604 GUALDA, G. A. R. & GHIORSO, M. S. 2007. Magnetite scavenging and the buoyancy of
605 bubbles in magmas. Part 2: Energetics of crystal-bubble attachment in magmas. Contributions to
606 Mineralogy and Petrology, 154, 479–490.

607 HIGGINS, M. D. 2006. Verification of ideal semi-logarithmic, lognormal or fractal crystal
608 size distributions from 2D datasets. Journal of Volcanology and Geothermal Research, 154, 1, 8–
609 16.

610 Huber, C., Bachmann, O., & Manga, M. 2010. Two competing effects of volatiles on heat
611 transfer in crystal-rich magmas: Thermal insulation vs defrosting. Journal of Petrology 51, 4, 847–
612 867.

613 FOROOZAN, R., ELSWORTH, D., VOIGHT, B., & MATTIOLI, G. S. 2010. Dual
614 reservoir structure at Soufrière Hills Volcano inferred from continuous GPS observations and
615 heterogeneous elastic modeling. Geophysical Research Letters, 37, 19.

GIACHETTI, T., DRUITT, T. H., BURGISSER, A., ARBARET, L. & GALVEN, C. 2010. Bubble nucleation, growth and coalesence during the 1997 Vulcanian explosions of Soufrière Hills Volcano, Montserrat. Journal of Volcanology and Geothermal Research, 193, 215–231.

HAMMER, J. E., CASHMAN, K. V., & VOIGHT, B. 2000. Magmatic processes revealed by textural and compositional trends in Merapi dome lavas. Journal of Volcanology and Geothermal Research, 100, 1, 165–192.

HAUTMANN, S., GOTTSMANN, J., SPARKS, R. S. J., COSTA, A., MELNIK, O. & VOIGHT, B. 2009. Modelling ground deformation caused by oscillating overpressure in a dyke conduit at Soufrière Hills Volcano, Montserrat. Tectonophysics, 471, 1, 87–95.

HIGGINS, M. D., & CHANDRASEKHARAM, D. 2007. Nature of sub-volcanic magma chambers, Deccan province, India: Evidence from quantitative textural analysis of plagioclase megacrysts in the Giant Plagioclase Basalts. Journal of Petrology, 48, 5, 885–900.

HUMPHREYS, M. C. S., CHRISTOPHER, T. & HARDS, V. 2009. Microlite transfer by disaggregation of mafic inclusions following magma mixing at Soufrière Hills Volcano, Montserrat. Contributions to Mineral Petrology, 157, 609–624.

HUMPHREYS, M. C. S., EDMONDS, M., CHRISTOPHER, T., & HARDS, V. (2009). Chlorine variations in the magma of Soufrière Hills Volcano, Montserrat: Insights from Cl in hornblende and melt inclusions. Geochimica et Cosmochimica Acta, 73, 19, 5693–5708.

HUMPHREYS, M. C. S., BROOKER, R. A., FRASER, D. G., BURGISSER, A., MANGAN, M. T. & MCCAMMON, C. 2014. Iron oxidation state in hydrous rhyolites during magma ascent and degassing. Journal of Petrology, in review.

HUPPERT, H. E., SPARKS, R. S. J., WHITEHEAD, J. A., & HALLWORTH, M. A. 1986. Replenishment of magma chambers by light inputs. Journal of Geophysical Research, Solid Earth 91, B6, 6113–6122.

HUPPERT, H. E., SPARKS, R. S. J., & TURNER, J. S. (1984). Some effects of viscosity on the dynamics of replenished magma chambers. Journal of Geophysical Research: Solid Earth 89, B8, 6857–6877.

HURWITZ, S. & NAVON, O. 1994. Bubble nucleation in rhyolitic melts: Experiments at high pressure, temperature and water content. Earth & Planetary Science Letters, 122, 267–280.

JERRAM, D. A., CHEADLE, M. J., HUNTER, R. H., & ELLIOTT, M. T. 1996. The spatial distribution of grains and crystals in rocks. Contributions to Mineralogy and Petrology, 125, 1, 60–74.

JERRAM, D. A., CHEADLE, M. J., & PHILPOTTS, A. R. 2003. Quantifying the building blocks of igneous rocks: are clustered crystal frameworks the foundation? Journal of Petrology, 44, 11, 2033–2051.

KIDDLE, E. J. 2011. The structure of the crust and magmatic system at Montserrat, Lesser Antilles. PhD thesis, University of Bristol.

KLUG, C., & CASHMAN, K. V. 1996. Permeability development in vesiculating magmas: implications for fragmentation. Bulletin of Volcanology, 58, 2–3, 87–100.

KRETZ, R. 1966. Interpretation of the shape of mineral grains in metamorphic rocks. Journal of Petrology, 7, 1, 68–94.

LARSEN, J. F., DENIS, M.-H. & GARDNER, J. E. 2004. Experimental study of bubble coalescence in rhyolitic and phonolitic melts. Geochimica et Cosmochimica Acta 68, 2, 333–344.

MANGAN, M. & SISSON, T. 2005. Evolution of melt-vapor surface tension in silicic volcanic systems: experiments with hydrous melts. Journal of Geophysical Research, 110, B01202.

MARTIN, V. M., HOLNESS, M. B., & PYLE, D. M. 2006. Textural analysis of magmatic enclaves from the Kameni Islands, Santorini, Greece. Journal of Volcanology and Geothermal Research, 154, 1, 89–102.

MOUSSALLAM, Y., OPPENHEIMER, C., SCAILLET, B., GAILLARD, F., KYLE, P., PETERS, N., HARTLEY, M., BERLO, K. & DONOVAN, A. 2014. Tracking the oxidation state of Erebus magmas, from mantle to surface, driven by magma ascent and degassing. Earth and Planetary Science Letters 393, 200–209.

MURPHY, M. D., SPARKS, R. S. J., BARCLAY, J., CARROLL, M. R. & BREWER, T. S. 2000. Remobilization of andesite magma by intrusion of mafic magma at the Soufrière Hills Volcano, Montserrat, West Indies. Journal of Petrology, 41, 21–42.

NAKAMURA, M. 1995. Continuous mixing of crystal mush and replenished magma in the ongoing Unzen eruption. Geology 23, 9, 807–810.

PHILLIPS, J. C., & WOODS, A. W. 2002. Suppression of large-scale magma mixing by melt–volatile separation. Earth and Planetary Science Letters 204, 1, 4–60.

PHILLIPS, J. C. & WOODS, A. W. 2001. Bubble plumes generated during recharge of basaltic magma reservoirs. Earth and Planetary Science Letters 186, 2, 297–309.

PLAIL, M., BARCLAY, J., HUMPHREYS, M. C. S., EDMONDS, M., HERD, R. A. & CHRISTOPHER, T., 2014. Characterisation of mafic enclaves in the erupted products of Soufrière

679 Hills Volcano, Montserrat 1995-2010. In: The eruption of Soufriere Hills Montserrat from 2000 to
680 2010. Eds G. Wadge, R. Robertson, B. Voight. Geological Society, London, Memoirs, 39, 341–358.

681 PLANK, T., KELLEY, K. A., ZIMMER, M. M., HAURI, E. H. & WALLACE, P. J. 2013.
682 Why do mafic arc magmas contain~ 4wt% water on average? Earth and Planetary Science Letters
683 364, 168–179.

684 RIDOLFI, F., RENZULLI, A. & PUERINI, M. 2010. Stability and chemical equilibrium of
685 amphibole in calc-alkaline magmas: an overview, new thermobarometric formulations and
686 application to subduction-related volcanoes. Contributions to Mineralogy and Petrology 160, 1 45–
687 66.

688 RUDGE, J. F., HOLNESS, M. B., & SMITH, G. C. 2008. Quantitative textural analysis of
689 packings of elongate crystals. Contributions to Mineralogy and Petrology, 156, 4, 413–429.

690 RUPRECHT, P., BERGANTZ, G. W. & DUFEK, J. 2008. Modeling of gas-driven
691 magmatic overturn: Tracking of phenocryst dispersal and gathering during magma mixing.
692 Geochemistry, Geophysics, Geosystems 9, 7.

693 SCHÄFER, F. N. & FOLEY, S. F. 2002. The effect of crystal orientation on the wetting
694 behaviour of silicate melts on the surfaces of spinel peridotite minerals. Contributions to
695 Mineralogy and Petrology, 143, 254–261.

696 SCHEU, B., SPIELER, O., & DINGWELL, D. B. 2006. Dynamics of explosive volcanism
697 at Unzen volcano: an experimental contribution. Bulletin of volcanology, 69, 2, 175–187.

698 STASIUK, M. V., BARCLAY, J., CARROLL, M. R., JAUPART, C., RATTÉ, J. C.,
699 SPARKS, R. S. J., & TAIT, S. R. 1996. Degassing during magma ascent in the Mule Creek vent
700 (USA). Bulletin of Volcanology, 58, 2-3, 117–130.

701 THOMAS, N., TAIT, S. & KOYAGUCHI, T. 1993. Mixing of stratified liquids by the
702 motion of gas bubbles: application to magma mixing. Earth and Planetary Science Letters 115, 1
703 161–175.

704 WADGE, G., VOIGHT, B., SPARKS, R.S.J., COLE, P., LOUGHLIN, S.C., 2014. An
705 Overview of the Eruption of Soufrière Hills Volcano from 2000-2010. In: The eruption of Soufriere
706 Hills Montserrat from 2000 to 2010. Eds G. Wadge, R. Robertson, B. Voight. Geological Society,
707 London, Memoirs, 39.

708 WALLACE, P. J. 2001. Volcanic SO_2 emissions and the abundance and distribution of
709 exsolved gas in magma bodies. Journal of Volcanology and Geothermal Research 108, 1, 85–106.

710

FIGURE CAPTIONS

Figure 1: Two possible configurations of bubble, liquid and crystal. On the left, the bubble is entirely within the liquid; on the right it is attached to the crystal. The schematic diagram of the melt-bubble-crystal junction indicates the balance of forces, with surficial energies (σ), the wetting angle Ψ and the bubble-mineral angle θ. Modified from Gualda and Ghiorso (2007).

Figure 2: Photographs of lava blocks in the field. Lava blocks were emplaced by a pyroclastic flow on 7 January 2007 from Soufrière Hills Volcano in the Belham River Valley, Montserrat. The blocks are a few metres in dimension (a), made of porphyritic andesite, with small mafic enclaves (shown in (b)) of basaltic to basaltic andesite composition. Hammer in (a) 47 cm long.

Figure 3: Representative backscattered electron images from the Scanning Electron Microscope: a-c show mafic enclaves, d shows porous andesite, all labelled with sample number. Phases are labelled: mgt: magnetite; ves: vesicle; amph: amphibole; opx: orthopyroxene; plag: plagioclase; gl: glass.

Figure 4: Synthetic point patterns to show two independent populations and their associated statistics. Left: point patterns to show the spatial arrangement of the two populations, each labelled with the characteristics of each population (random, clustered etc; described in text). Plots from left to right: cumulative probability distribution to show Nearest Neighbour Distances, in microns; a plot of Ripley's L Function against distance, r, in microns; the Pair Correlation Function against distance, r, in microns. Also shown in each plot, as grey shading, are the results of 100 random (poisson) point pattern simulations. Plots generated using the Spatstat package in R.

Figure 5: Synthetic point patterns to show two dependent populations and their associated statistics. Left: point patterns to show the spatial arrangement of the two populations, each labelled with the characteristics of each population (random, clustered etc; described in text). An explanation of how the second population is generated using seed positions from the first population is given in the text. Plots from left to right: cumulative probability distribution to show Nearest Neighbour Distances, in microns; a plot of Ripley's L Function against distance, r, in microns; a plot to show the Pair Correlation Function against distance, r, in microns. Also shown in each plot, as grey shading, are the results of 100 random (poisson) point pattern simulations. Plots generated using the Spatstat

744 package in R.

745

746 **Figure 6**: The effect of changing the order of the spatial analysis of the dependent populations in
747 the case of clustered-randomised or random-clustered distributions: a) the first population is
748 clustered and the second is linked spatially to the first, resulting in two clustered populations. The
749 nearest neighbour, Ripley's L and pair correlation functions (described in the text) shown strong
750 clustering; b) the first population is randomly distributed and the second is linked spatially to the
751 first population, resulting in the second population being weakly clustered. The nearest neighbour,
752 Ripley's L and pair correlation functions show clustering only on very small lengthscales and
753 ordering at intermediate lengthscales.

754

755 **Figure 7**: Bubble and magnetite size distributions for all of the samples studied. Curves are labelled
756 with sample name (Table 1) and sample type (andesite or mafic enclave). In general bubble size
757 distributions are shown in black, magnetite size distributions in red.

758

759 **Figure 8**: Vesicle area fraction (%, y axis) plotted against vesicle-free magnetite area fraction (%, x
760 axis). Andesite and mafic enclave samples are distinguished.

761

762 **Figure 9**: Representative statistical data for populations of magnetite and bubbles for a) one mafic
763 enclave sample and b) to e) andesite samples. Plots from left to right: point pattern of bubbles
764 (white) and magnetite (black), alongside the backscattered images of the analysed areas; Nearest
765 Neighbour distances (G(r); black solid line) as a cumulative probability distribution with distance, r
766 in microns, showing distributions that lie inside the envelope (in grey) for 100 random simulations
767 (red dashed line shows the results for a theoretical random distribution); Ripley's L Function with
768 distance r; the Pair Correlation Function with distance r.

769

770 **Figure 10**: Representative statistical data for populations of magnetite and bubbles for mafic
771 enclave samples. Plots from left to right: point pattern of bubbles (white) and magnetite (black),
772 alongside the backscattered images of the analysed areas; Nearest Neighbour distances (G(r); black
773 solid line) as a cumulative probability distribution with distance, r in microns, showing distributions
774 that lie inside the envelope (in grey) for 100 random simulations (red dashed line shows the results
775 for a theoretical random distribution); Ripley's L Function with distance r; the Pair Correlation
776 Function with distance r.

Figure 11: Plot to show the pair correlation function (pcf) as a function of distance r (in microns) for all of the point patterns studied here, separated into their types: andesite (red) and mafic enclave (black). The horizontal black line shows the pcf for a theoretical random distribution, and the grey envelope, the result of 100 random simulations.

Figure 12: Statistical plots to show the relationship between the locations of pyroxenes and the locations of bubbles in sample MVO1560_1. The plots show that there is no statistical departure from random behaviour, showing no linked spatial patterns. Plots as described in figures 9 and 10.

Figure 13: Cartoon to illustrate the processes to explain the spatial association of magnetite and vesicles, and to show the effects of such an association on the fluid mechanics of magma mingling. Water-saturated basaltic magma underplates an andesite magma body. Bubbles nucleate on magnetite over other crystal phases (amphibole is likely also a liquidus phase). The low viscosity of the melt and the significant fraction of exsolved vapour allow bubbles to rise up to the interface between the two magmas, sweeping up magnetite grains in the process. Bubbles and magnetite aggregates accumulate at the interface between the two magmas. Instabilities at the interface allow mafic enclaves to form and become incorporated into the andesite body. The enclaves are enriched in both magnetite and bubbles relative to the bulk mafic magma at depth.

Sample name	***Description of sample***	***Size of pixel (microns) in analysed BSE image***
BR6a1	Mafic enclave; glassy groundmass and quenched margins; 1 closest to rim, 3 closest to core (Type A)	2.15
BR6a 2		
BR6a 3		1.46
BR10 1	Mafic enclave; crystalline groundmass, no quenched margins (Type B)	2.22
BR10 2		
BR11 1	Mafic enclave; partially crystalline groundmass, quenched margins (Type A)	2.22
BR11 2		1.11
BR 12 1	Mafic enclave; glassy groundmass and quenched margins (Type A)	1.11
BR 12 2		
BR 12 3		
MT19 1	Mafic enclave; glassy groundmass and quenched margins (Type A)	0.24
MT19 2	Andesite	
MT19 3	Andesite	0.12
MT19 4	Andesite	
MVO 1560 1	Andesite	0.24
MVO 1560 2	Andesite	0.12
MVO 1560 3	Andesite	0.24
MVO 1560 4	Mafic enclave; crystalline groundmass, no quenched margins (Type B)	
MVO 1587 1	Mafic enclave; crystalline groundmass, no quenched margins (Type B)	
MVO 1587 2	Andesite	
MVO 1592 1	Mafic enclave; crystalline groundmass, no quenched margins (Type B)	0.12
MVO 1592 2	Andesite	
MVO 1592 3	Andesite	0.24
MVO 1592 4	Mafic enclave; crystalline groundmass, no quenched margins (Type B)	

Table 1: Sample names, types (andesite or mafic enclave) and brief description. See text for descriptions of andesite and mafic enclave petrography. Types A and B after Plail et al. (2014).

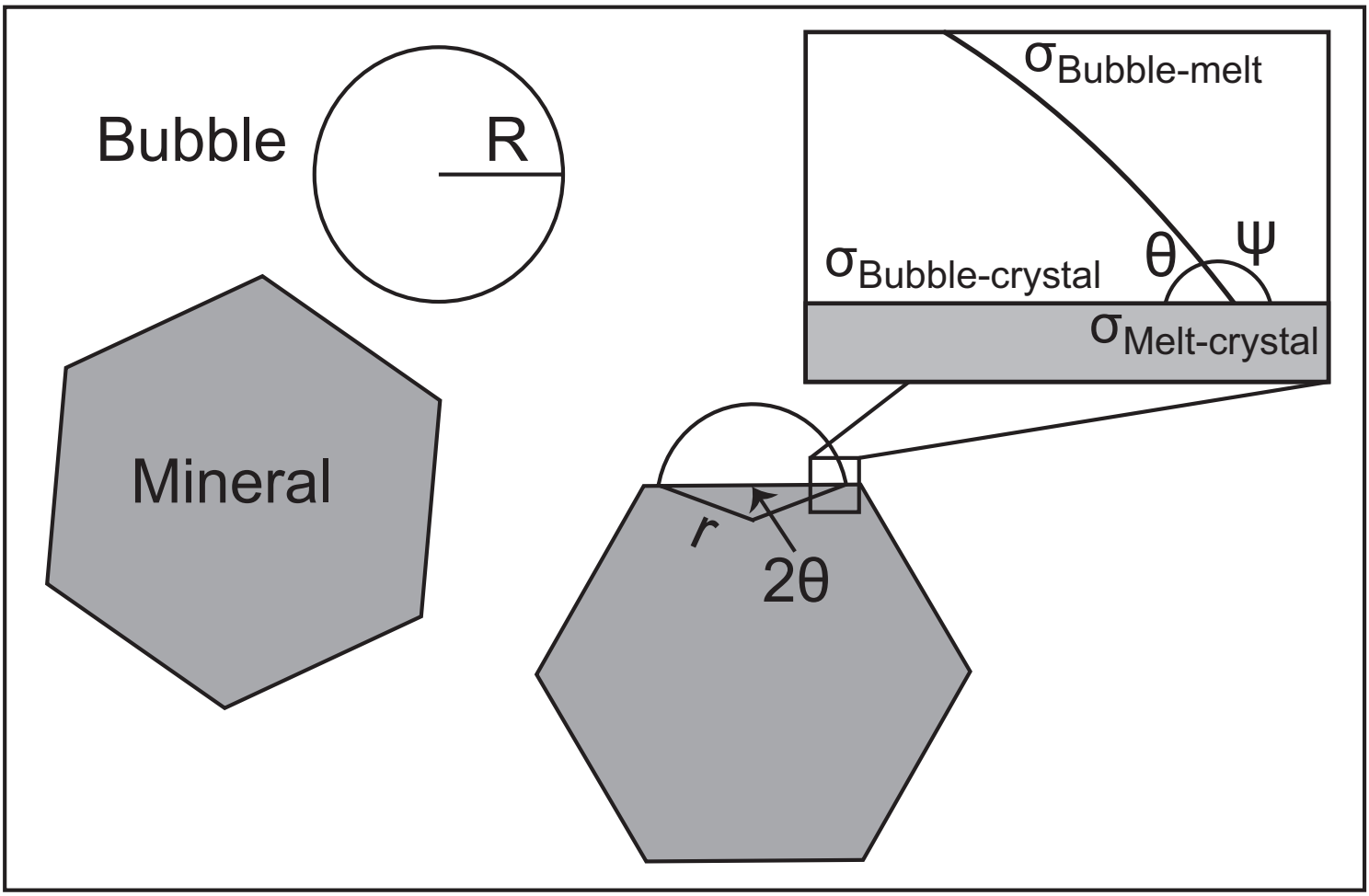
Bubble
R
Mineral
σBubble-melt
σBubble-crystal
θ
ψ
σMelt-crystal
r
2θ

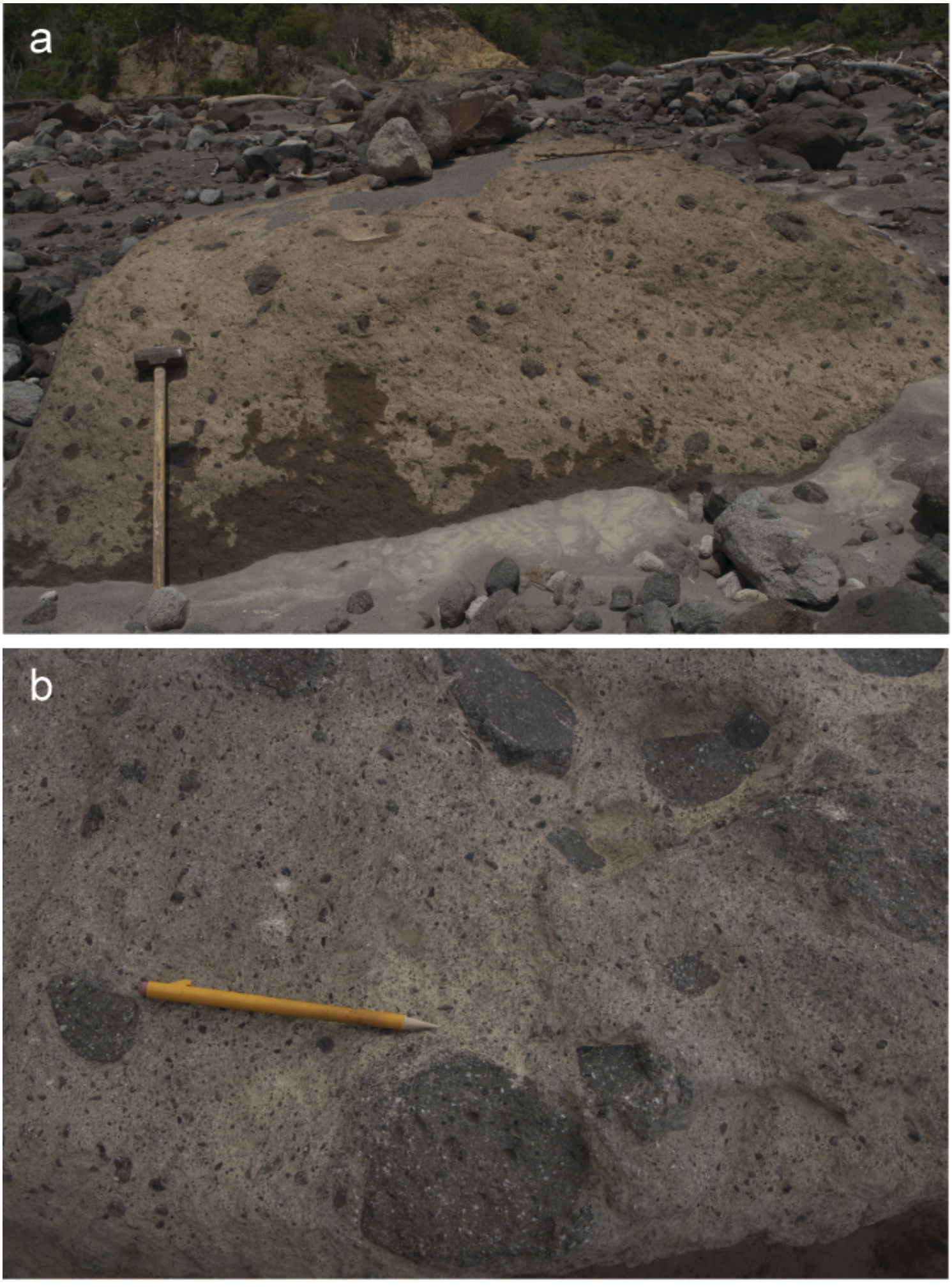
a
b

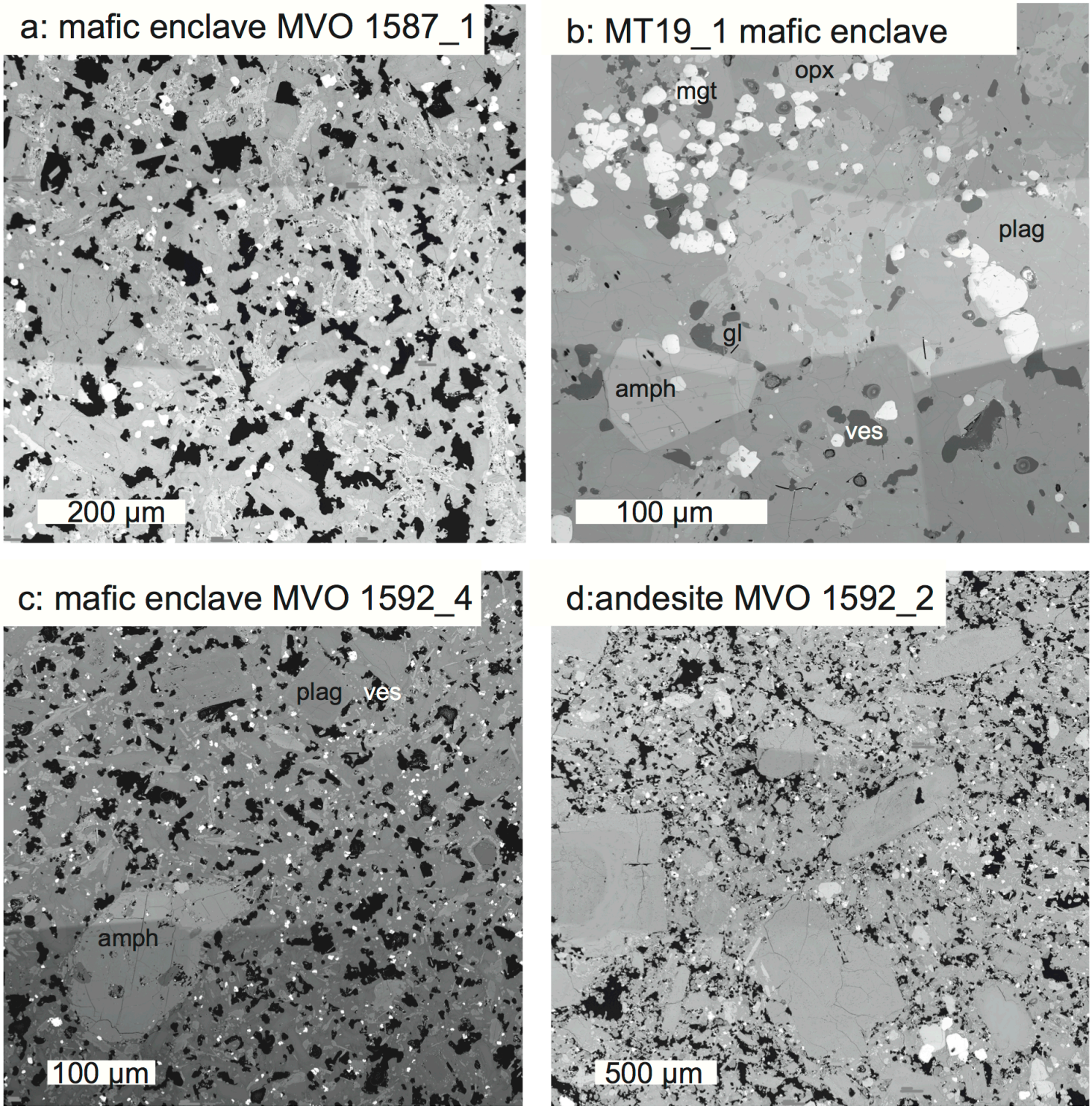
a: mafic enclave MVO 1587_1
200 µm
b: MT19_1 mafic enclave
opx
mgt
plag
gl
amph
ves
100 µm
c: mafic enclave MVO 1592_4
plag
ves
amph
100 µm
d:andesite MVO 1592_2
500 µm

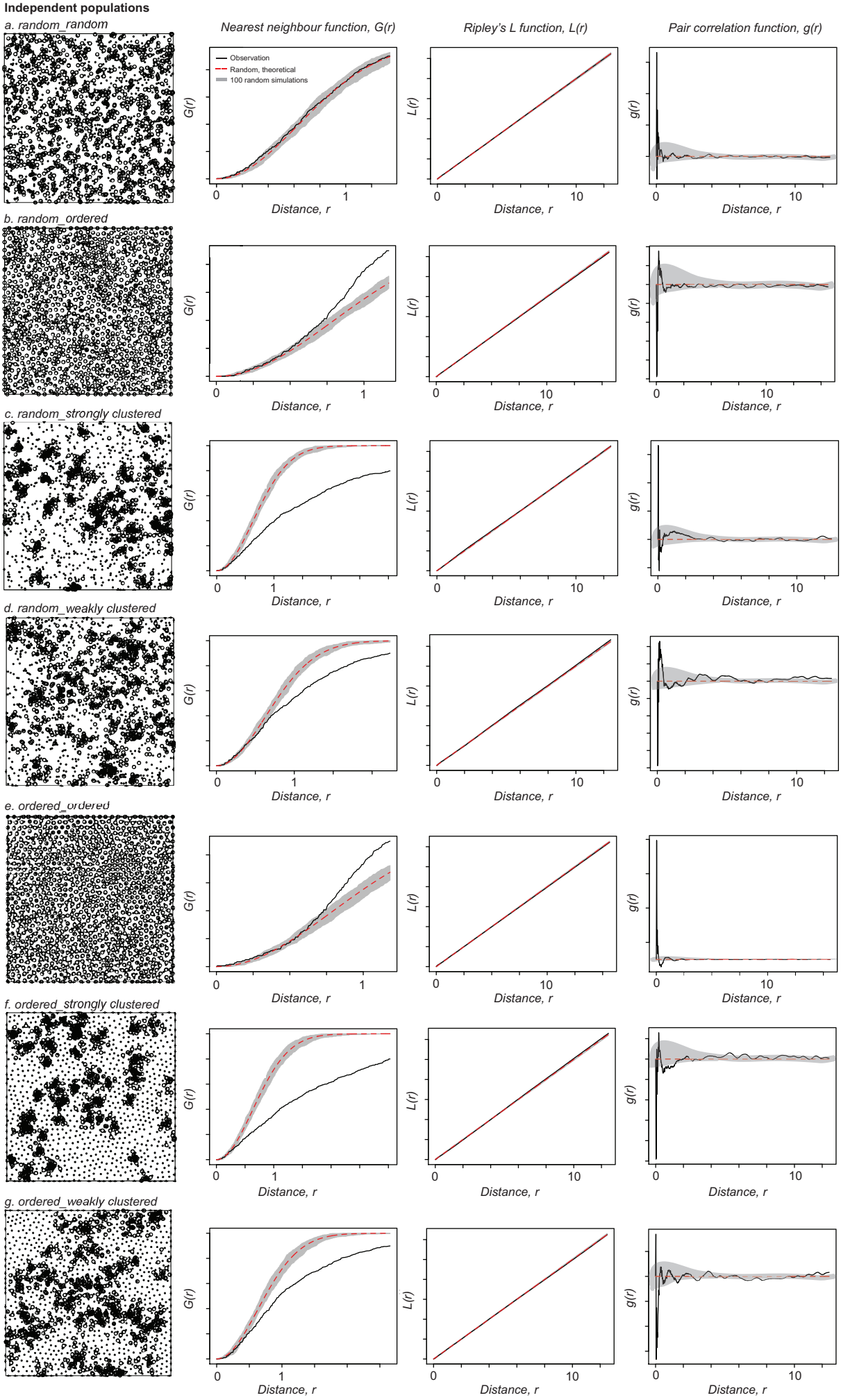
Independent populations
a. random_random
b. random_ordered
c. random_strongly clustered
d. random_weakly clustered
e. ordered_ordered
f. ordered_strongly clustered
g. ordered_weakly clustered
Nearest neighbour function, G(r)
Ripley's L function, L(r)
Pair correlation function, g(r)
Observation
Random, theoretical
100 random simulations
G(r)
L(r)
g(r)
Distance, r
0
1
10

Independent populations, cont.

h. weakly-clustered_weakly-clustered

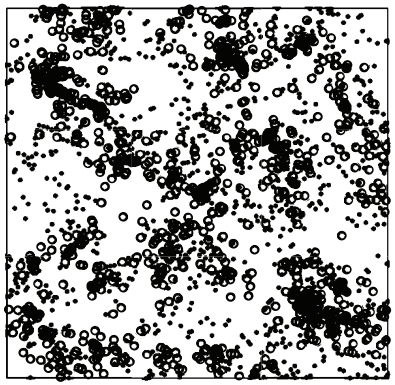

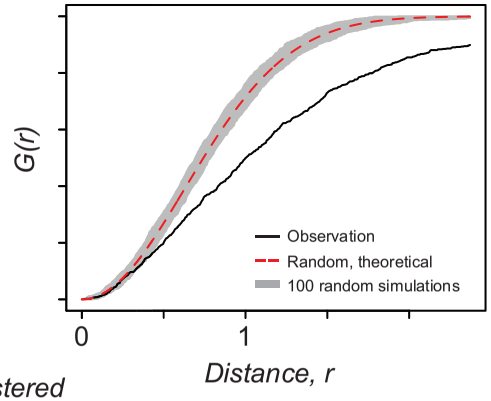

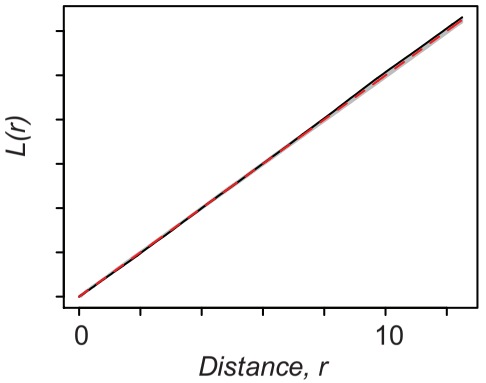

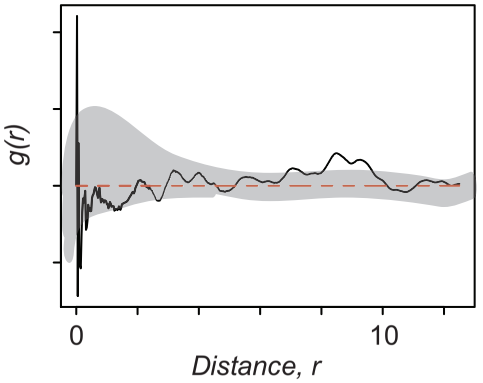

i. strongly-clustered_weakly-clustered

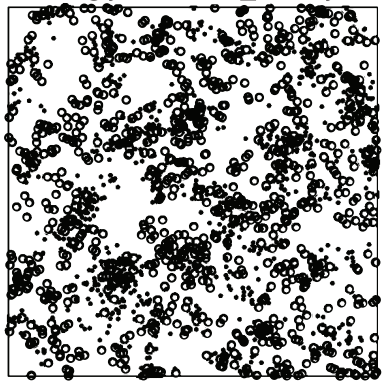

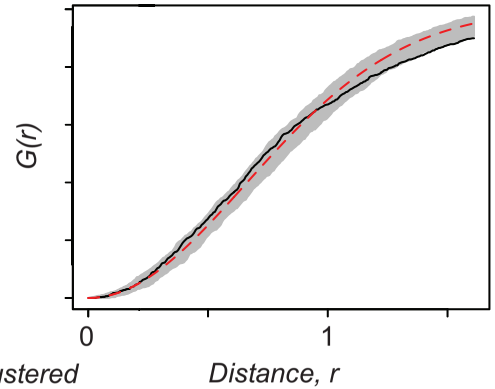

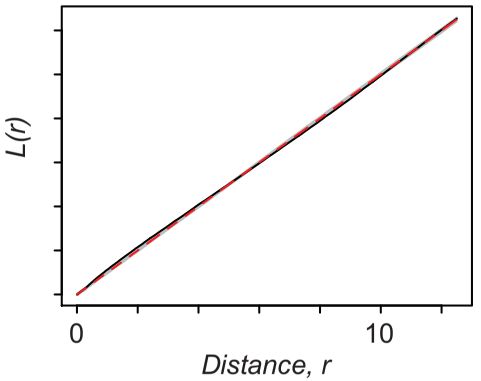

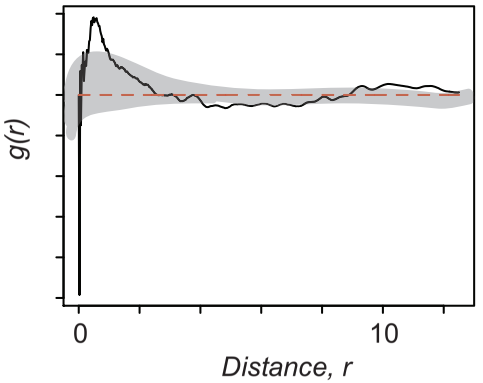

j. strongly-clustered_strongly-clustered

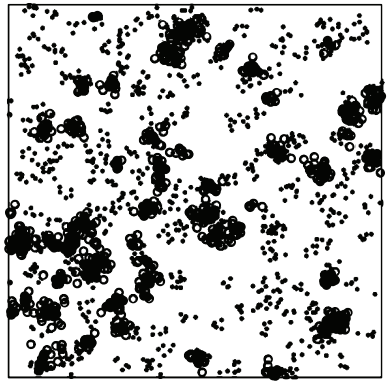

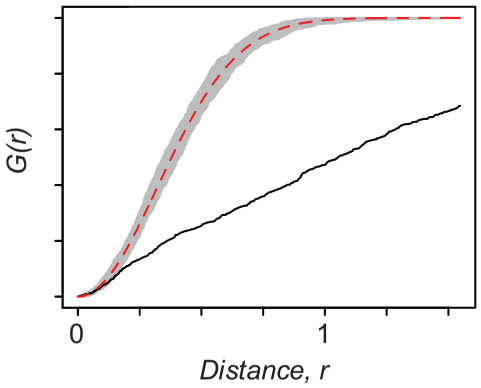

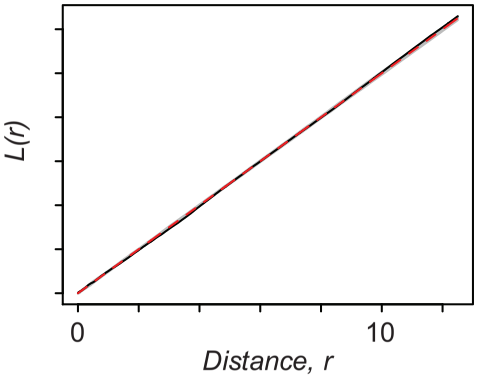

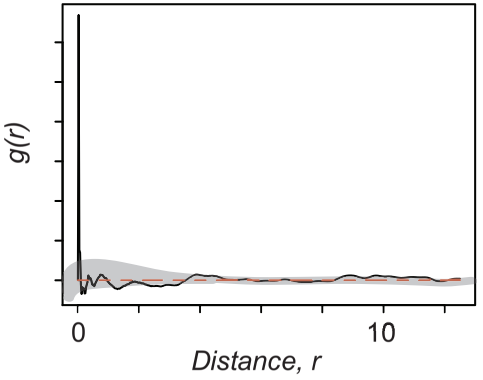

Dependent populations

a. weakly-clustered_weakly-clustered

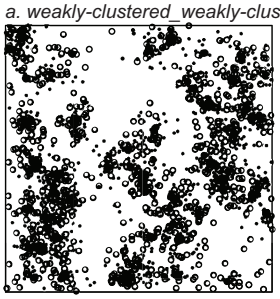

Nearest neighbour function, G(r)

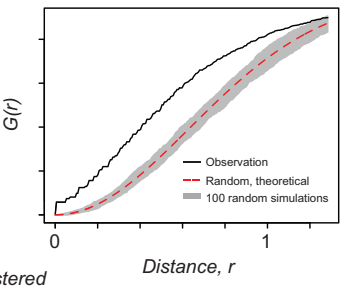

Ripley's L function, L(r)

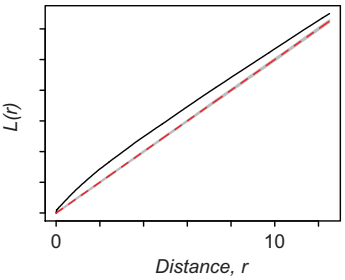

Pair correlation function, g(r)

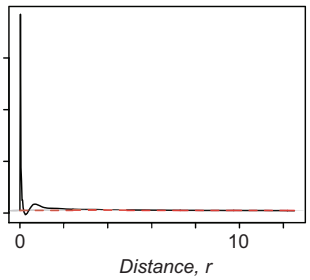

b. strongly-clustered_weakly-clustered

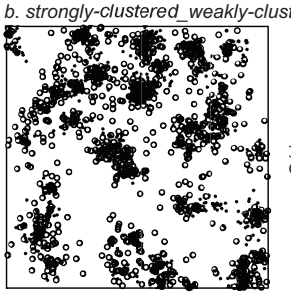

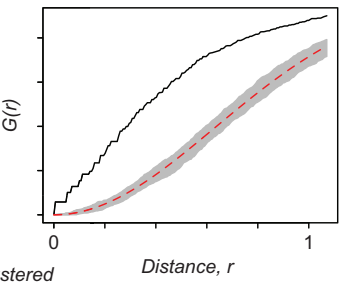

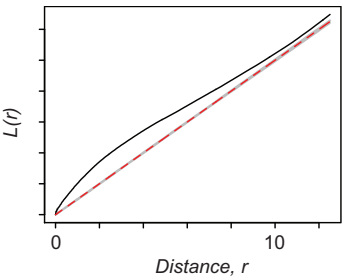

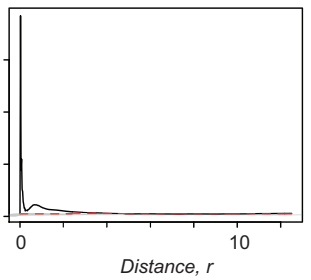

c. strongly-clustered_strongly-clustered

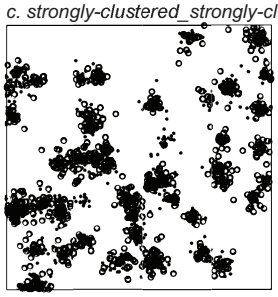

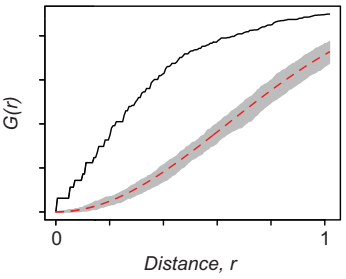

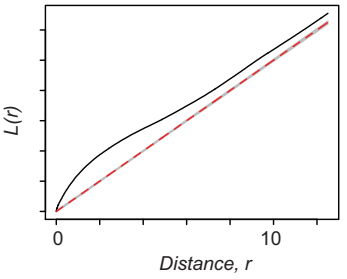

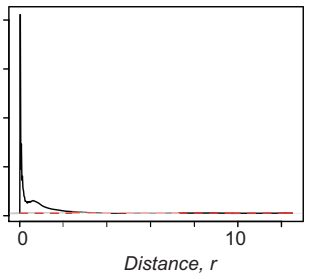

d. ordered_weakly-clustered

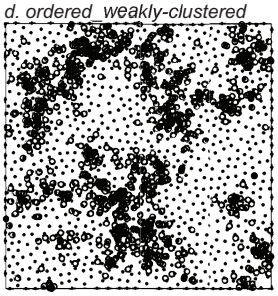

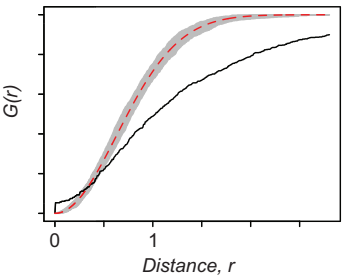

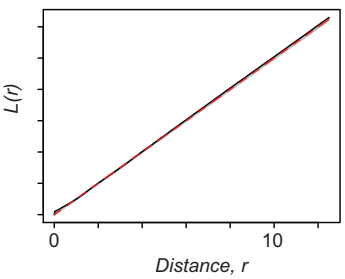

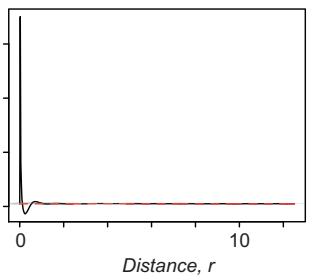

e. ordered_strongly-clustered

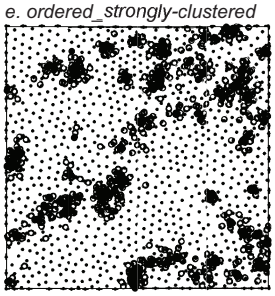

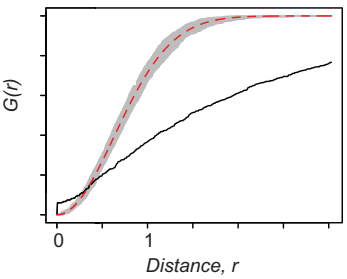

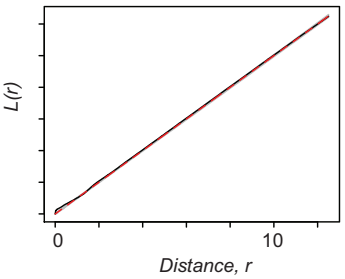

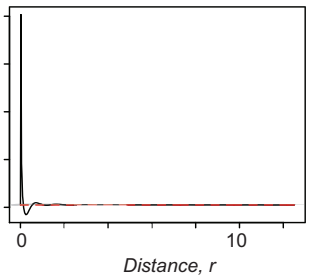

f. ordered_randomised

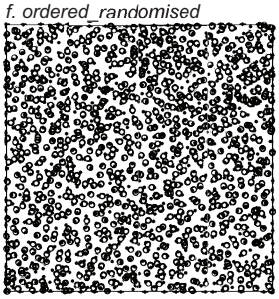

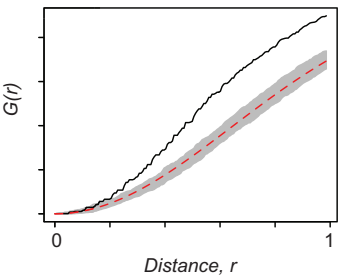

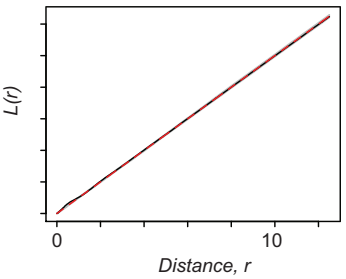

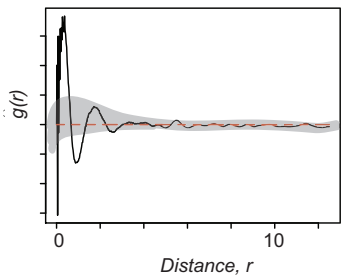

Dependent populations, cont.

g. random_weakly-clustered

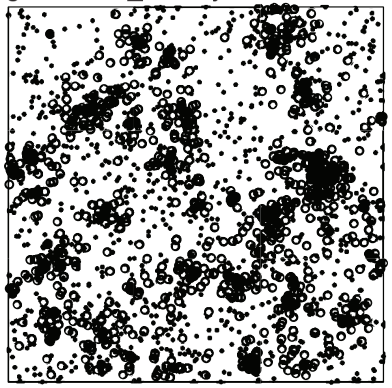

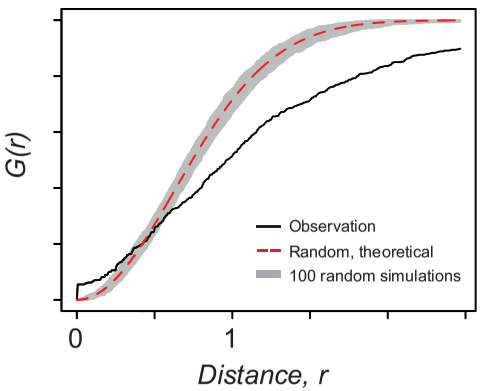

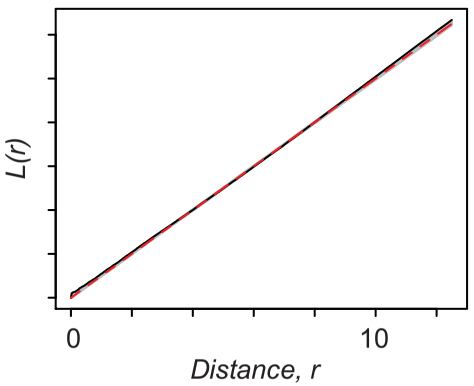

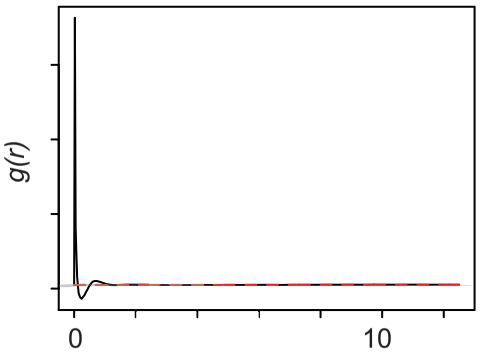

h. random_strongly-clustered

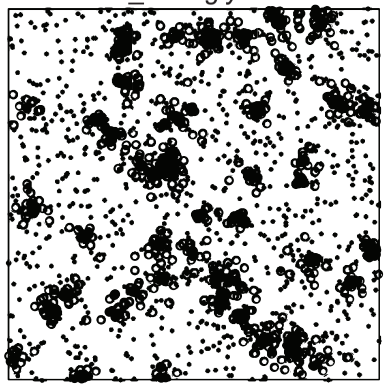

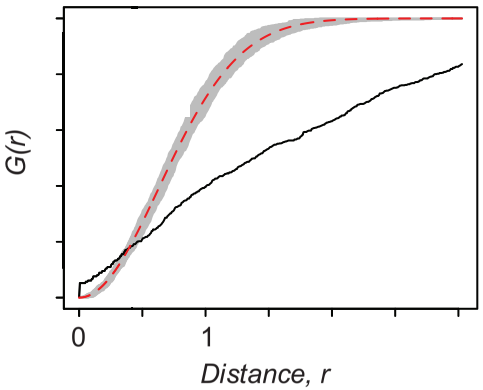

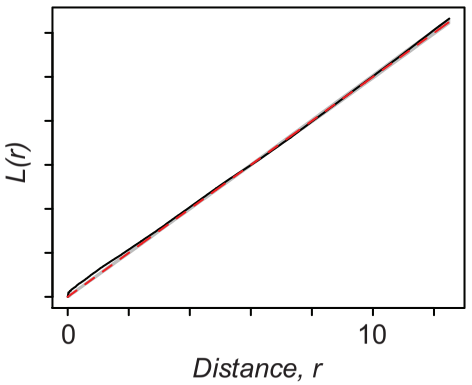

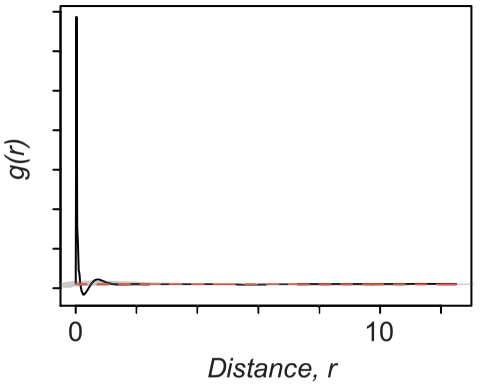

i. random_randomised

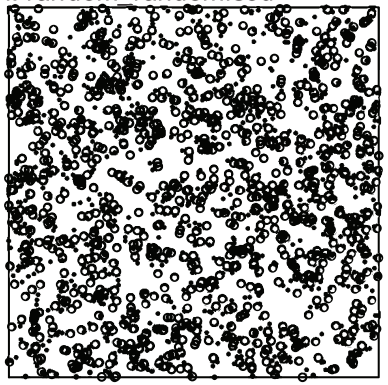

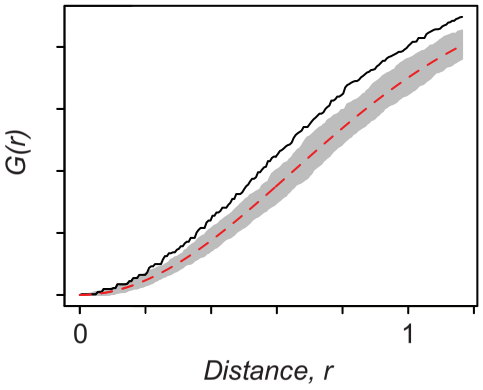

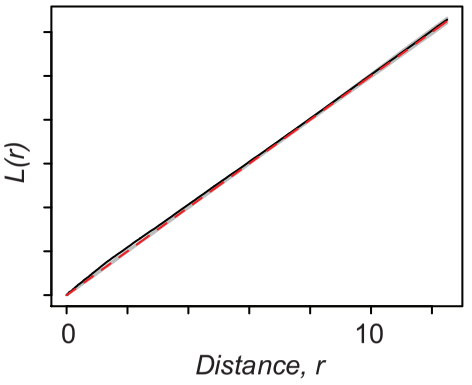

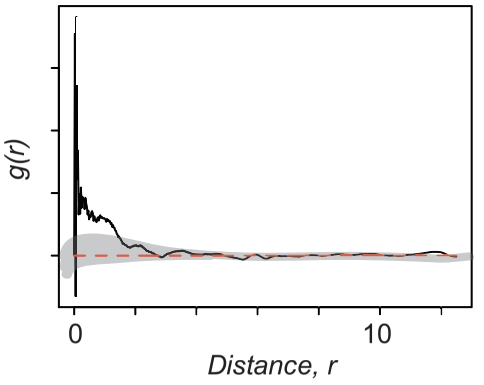

Dependent populations - changing the order of the analysis

a. weakly-clustered_randomised

e.g. bubbles nucleating on clustered magnetites

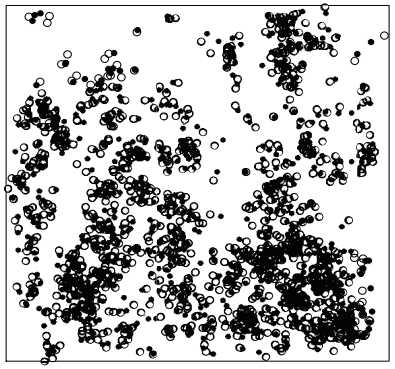

Nearest neighbour function, G(r)

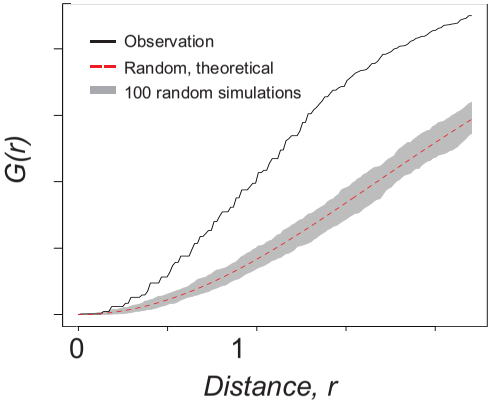

Ripley's L function, L(r)

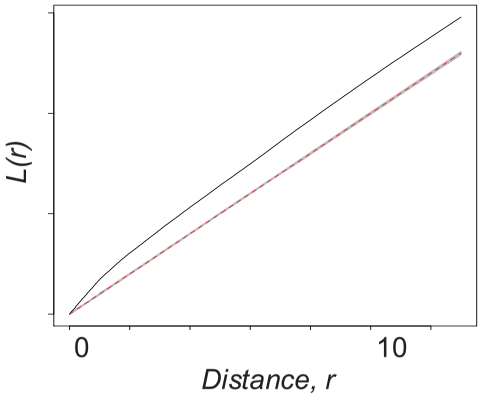

Pair correlation function, g(r)

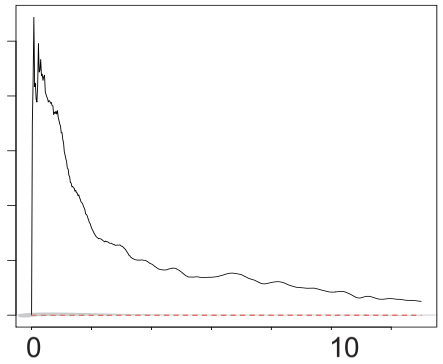

b. random_weakly-clustered

e.g. bubbles nucleating on random magnetites

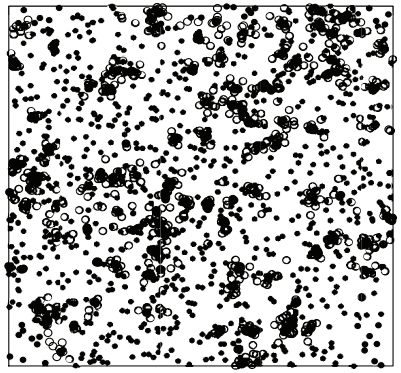

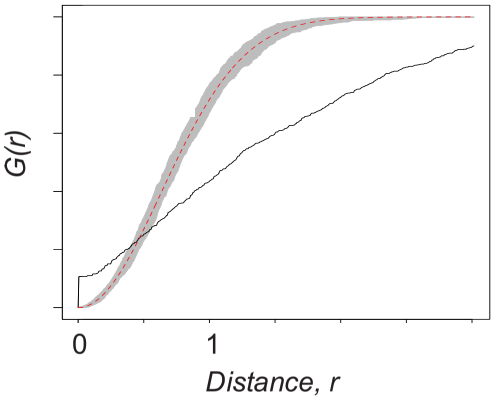

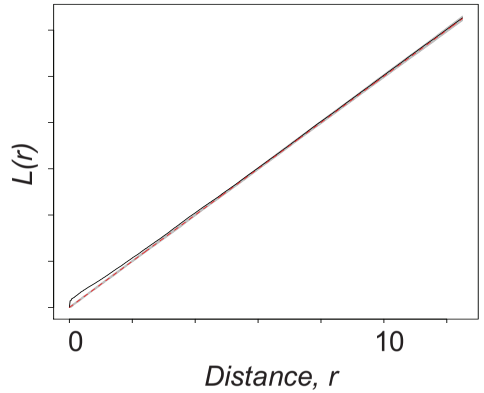

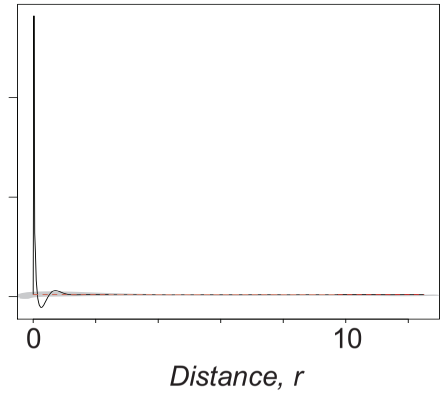

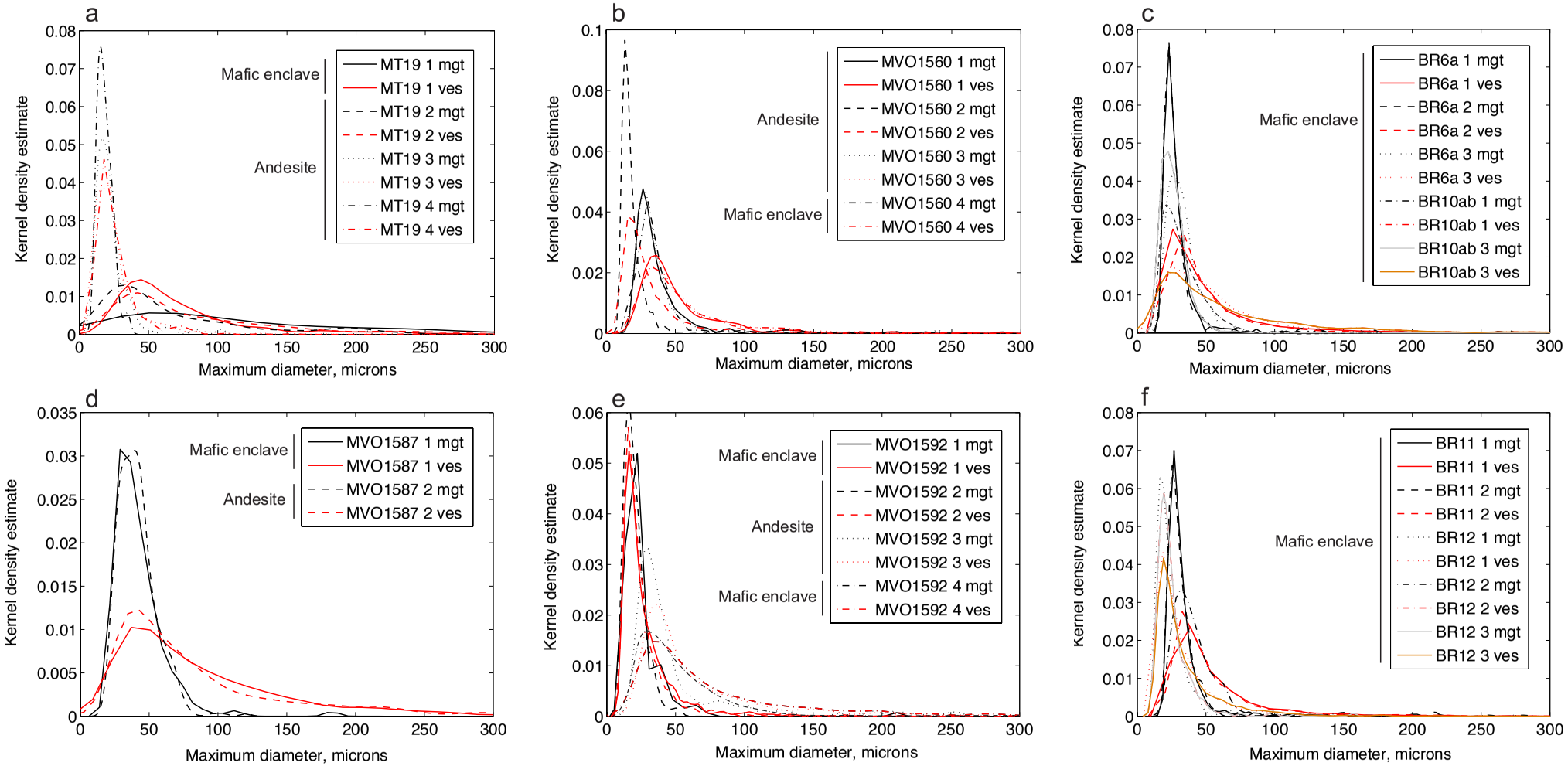
a
Kernel density estimate
Maximum diameter, microns
Mafic enclave
Andesite
MT19 1 mgt
MT19 1 ves
MT19 2 mgt
MT19 2 ves
MT19 3 mgt
MT19 3 ves
MT19 4 mgt
MT19 4 ves
b
Kernel density estimate
Maximum diameter, microns
Andesite
Mafic enclave
MVO1560 1 mgt
MVO1560 1 ves
MVO1560 2 mgt
MVO1560 2 ves
MVO1560 3 mgt
MVO1560 3 ves
MVO1560 4 mgt
MVO1560 4 ves
c
Kernel density estimate
Maximum diameter, microns
Mafic enclave
BR6a 1 mgt
BR6a 1 ves
BR6a 2 mgt
BR6a 2 ves
BR6a 3 mgt
BR6a 3 ves
BR10ab 1 mgt
BR10ab 1 ves
BR10ab 3 mgt
BR10ab 3 ves
d
Kernel density estimate
Maximum diameter, microns
Mafic enclave
Andesite
MVO1587 1 mgt
MVO1587 1 ves
MVO1587 2 mgt
MVO1587 2 ves
e
Kernel density estimate
Maximum diameter, microns
Mafic enclave
Andesite
Mafic enclave
MVO1592 1 mgt
MVO1592 1 ves
MVO1592 2 mgt
MVO1592 2 ves
MVO1592 3 mgt
MVO1592 3 ves
MVO1592 4 mgt
MVO1592 4 ves
f
Kernel density estimate
Maximum diameter, microns
Mafic enclave
BR11 1 mgt
BR11 1 ves
BR11 2 mgt
BR11 2 ves
BR12 1 mgt
BR12 1 ves
BR12 2 mgt
BR12 2 ves
BR12 3 mgt
BR12 3 ves

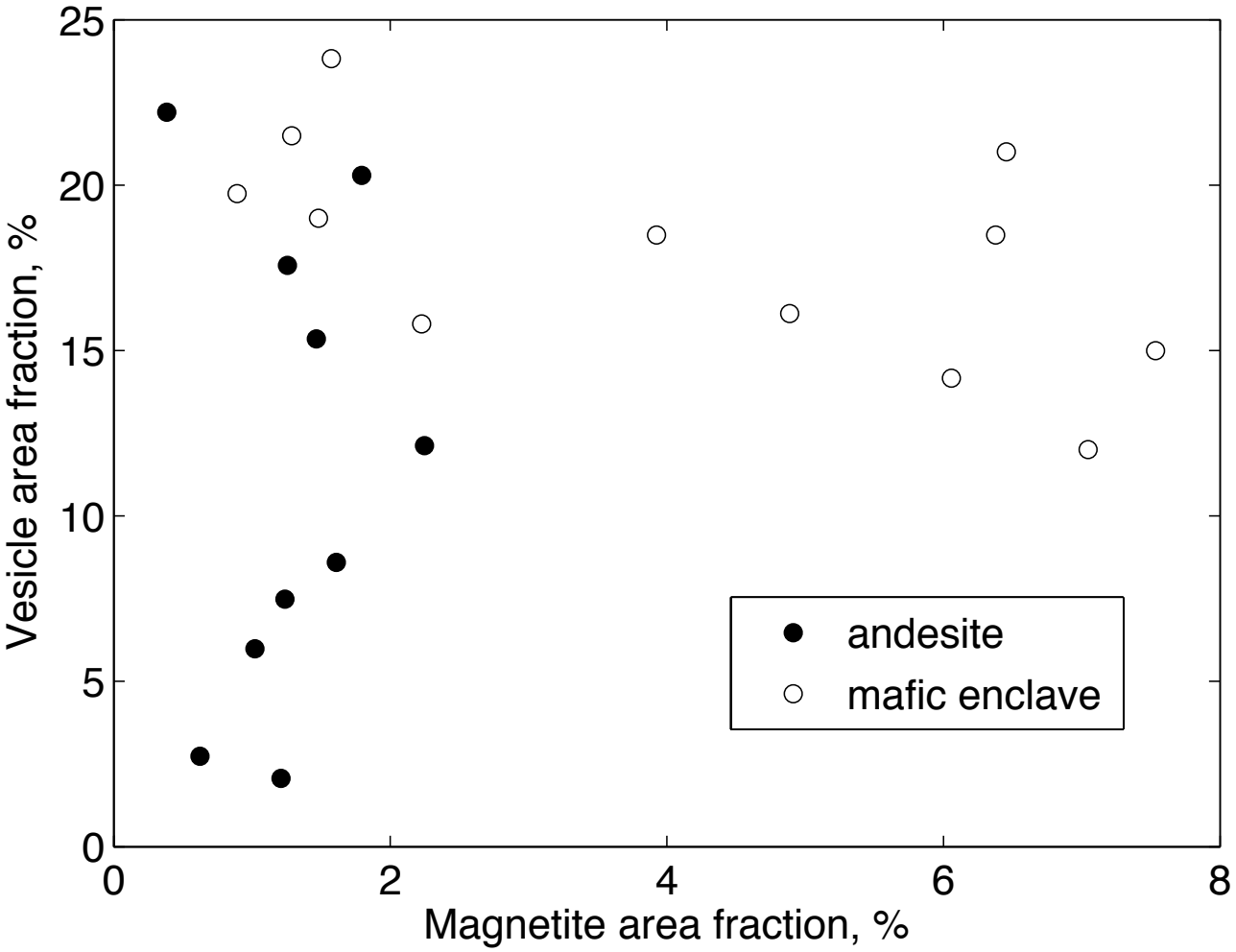
25
20
15
10
5
0
0
2
4
6
8
Vesicle area fraction, %
Magnetite area fraction, %
andesite
mafic enclave

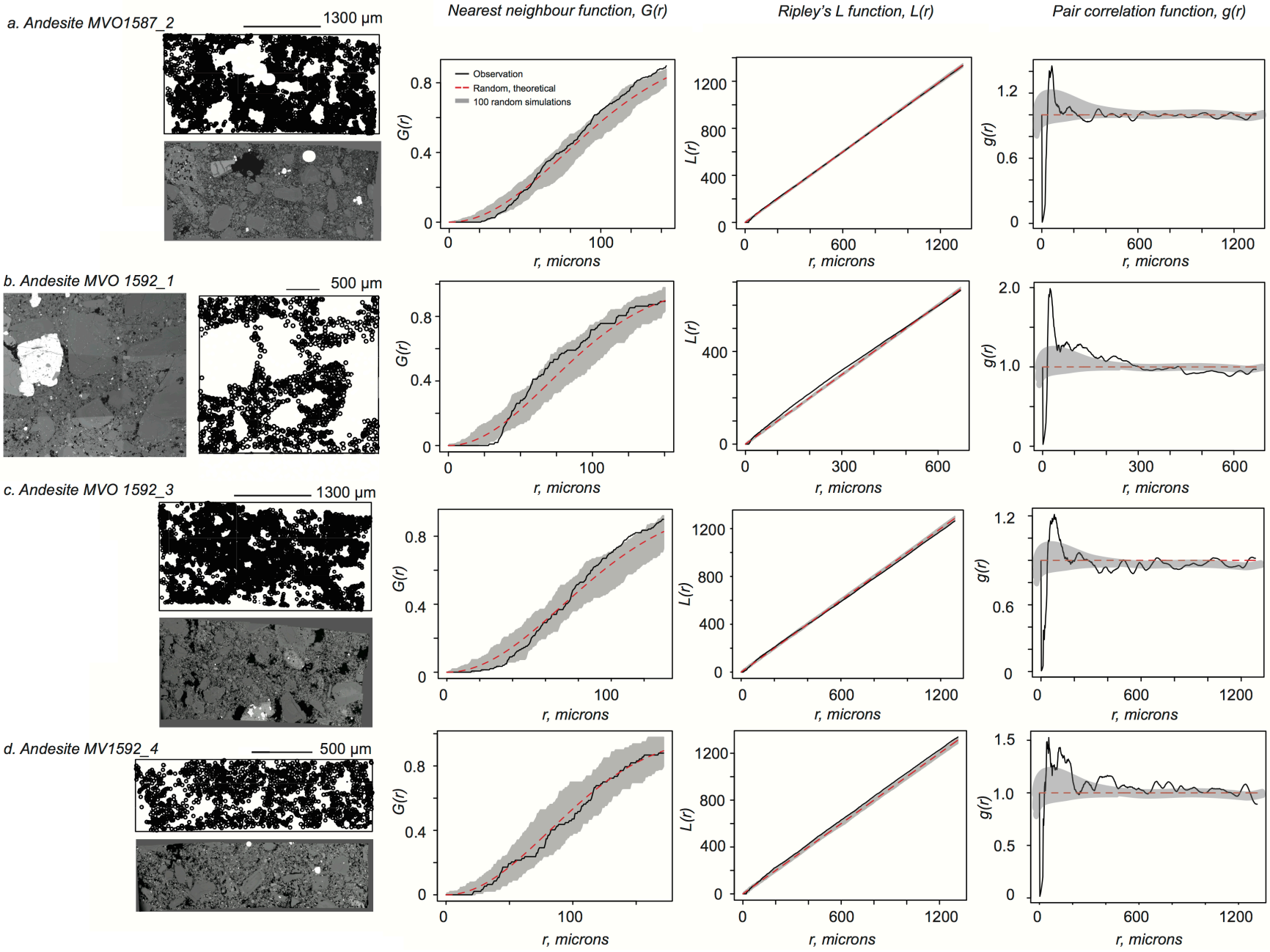
a. Andesite MVO1587_2
1300 µm
b. Andesite MVO 1592_1
500 µm
c. Andesite MVO 1592_3
1300 µm
d. Andesite MV1592_4
500 µm
Nearest neighbour function, G(r)
Ripley's L function, L(r)
Pair correlation function, g(r)
Observation
Random, theoretical
100 random simulations
G(r)
L(r)
g(r)
r, microns

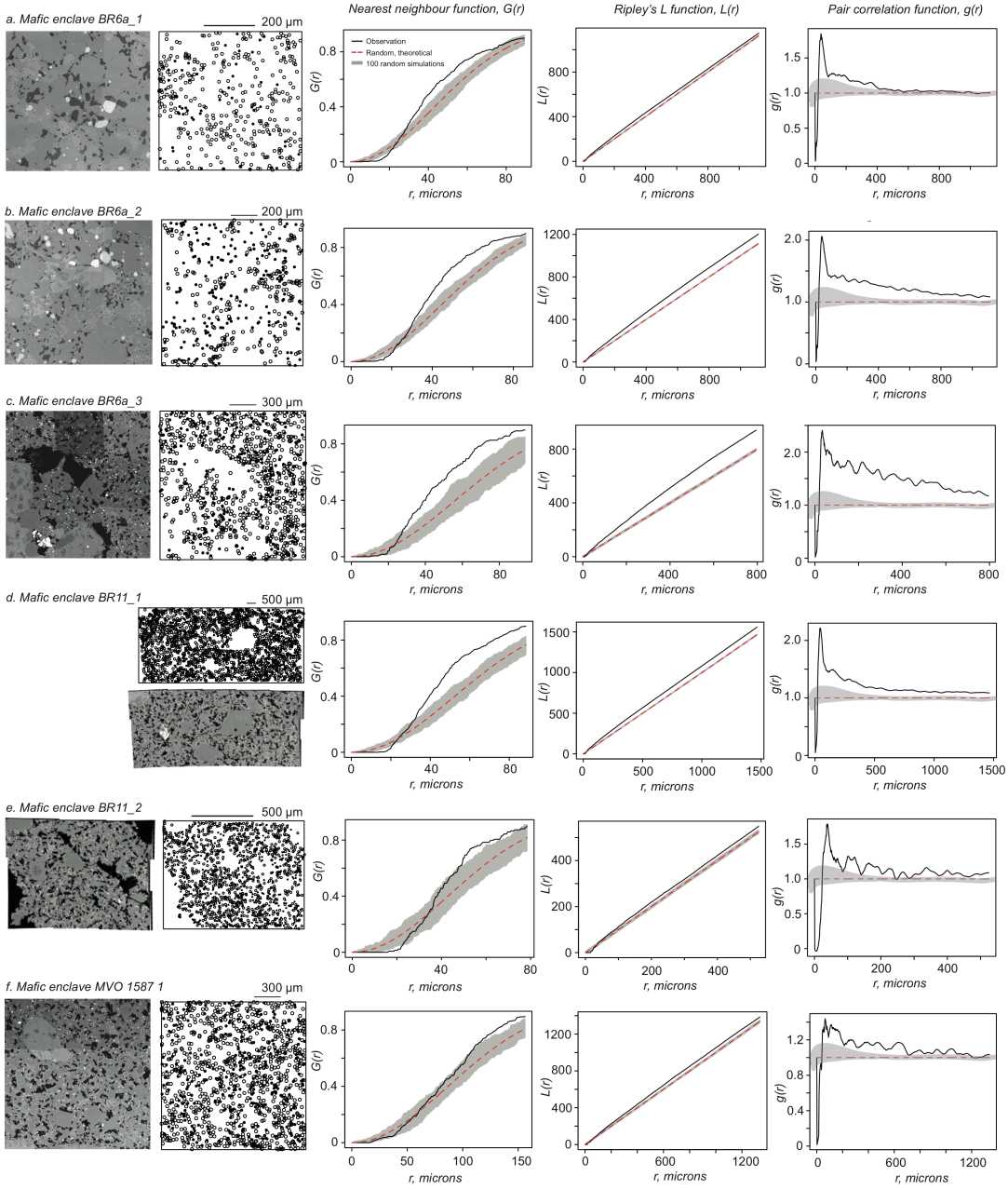
Nearest neighbour function, G(r)
Ripley's L function, L(r)
Pair correlation function, g(r)
a. Mafic enclave BR6a_1
200 µm
b. Mafic enclave BR6a_2
200 µm
c. Mafic enclave BR6a_3
300 µm
d. Mafic enclave BR11_1
500 µm
e. Mafic enclave BR11_2
500 µm
f. Mafic enclave MVO 1587 1
300 µm
Observation
Random, theoretical
100 random simulations
G(r)
L(r)
g(r)
r, microns

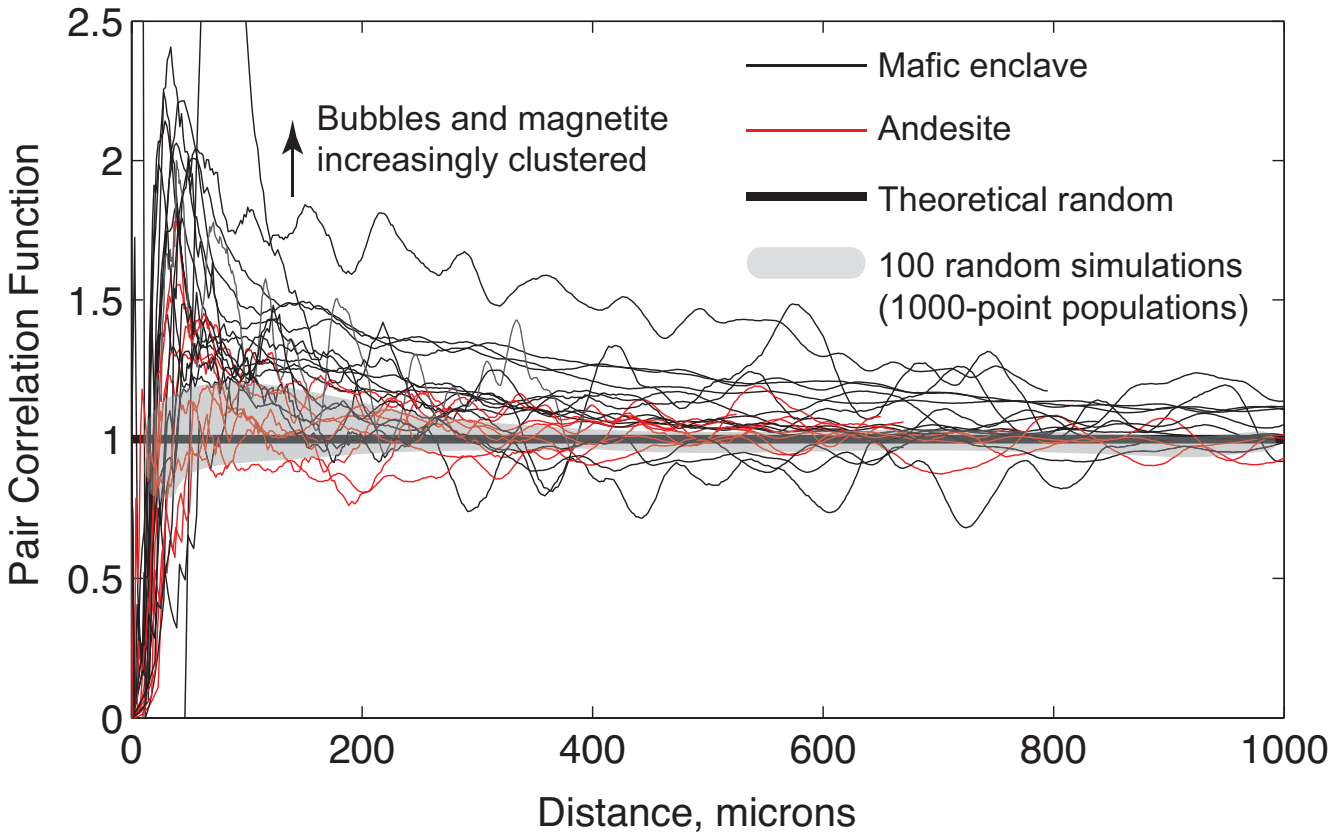
Pair Correlation Function
Distance, microns
Bubbles and magnetite
increasingly clustered
Mafic enclave
Andesite
Theoretical random
100 random simulations
(1000-point populations)
0
0.5
1
1.5
2
2.5
0
200
400
600
800
1000

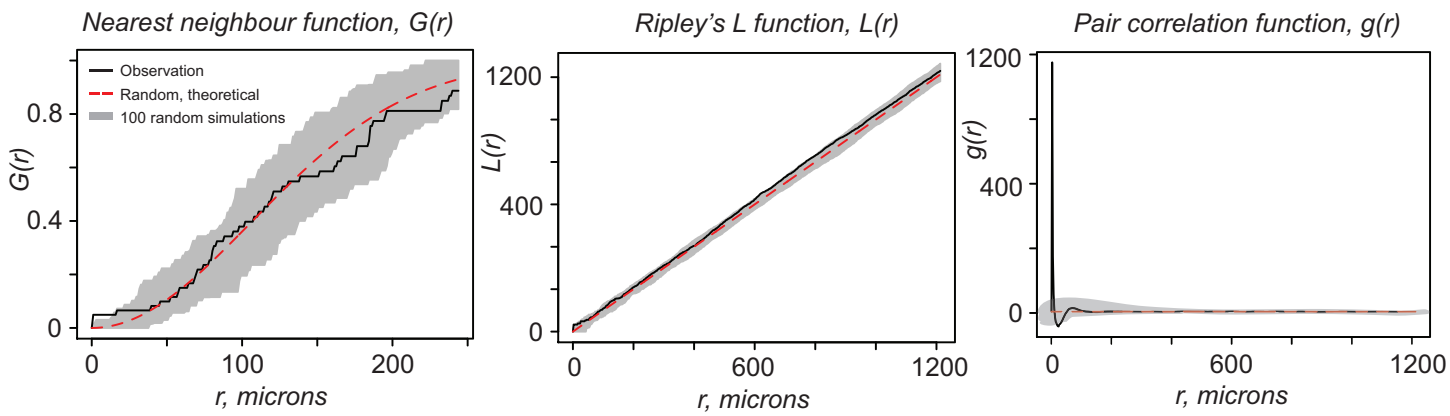
Nearest neighbour function, G(r)
Observation
Random, theoretical
100 random simulations
G(r)
0
0.4
0.8
0
100
200
r, microns
Ripley's L function, L(r)
L(r)
0
400
1200
0
600
1200
r, microns
Pair correlation function, g(r)
g(r)
0
400
1200
0
600
1200
r, microns

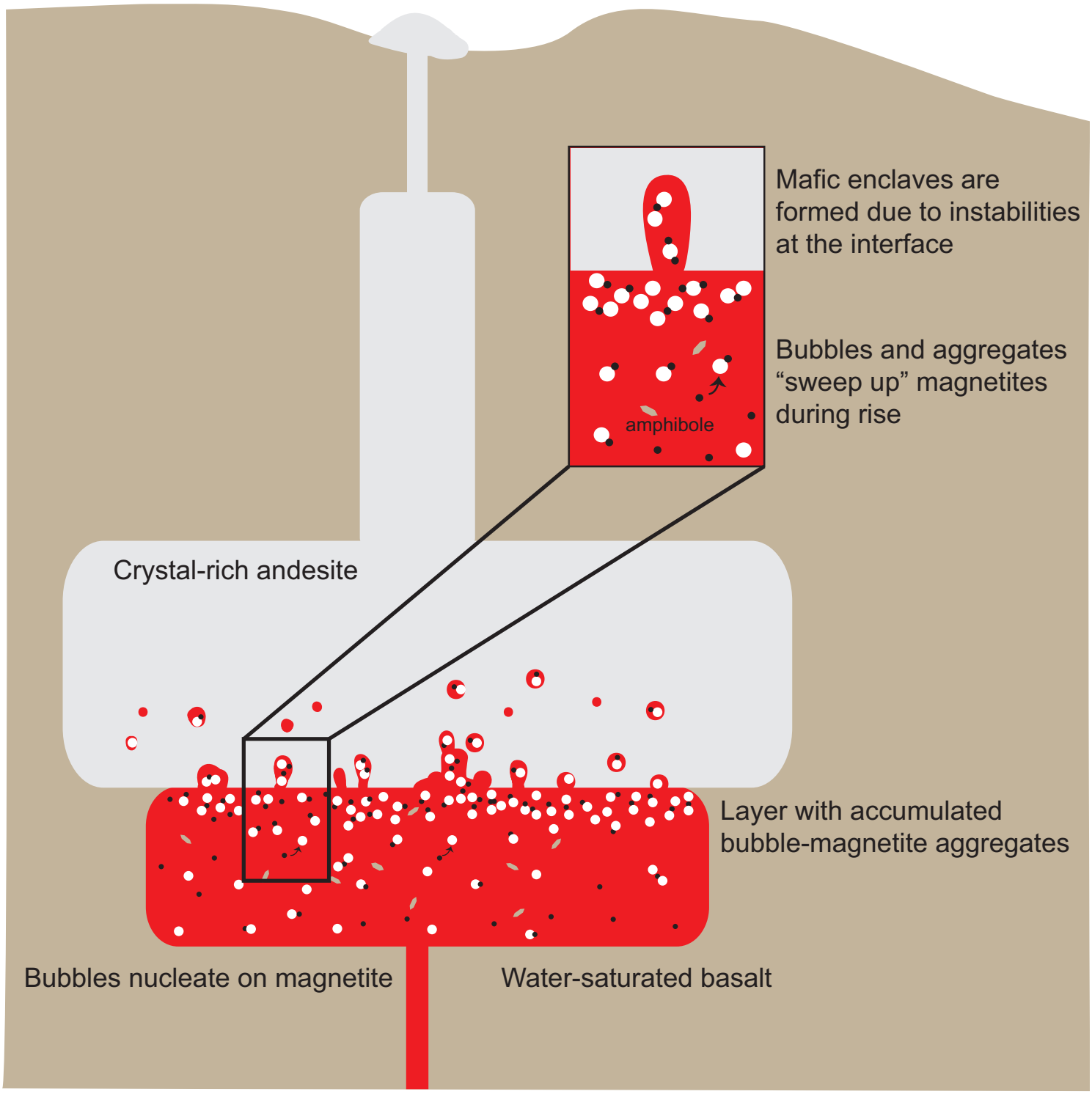
Mafic enclaves are formed due to instabilities at the interface
Bubbles and aggregates “sweep up” magnetites during rise
amphibole
Crystal-rich andesite
Layer with accumulated bubble-magnetite aggregates
Bubbles nucleate on magnetite
Water-saturated basalt